Application of Silicon-Based Thin Films in High-Efficiency Silicon Solar Cells for Carbon Neutrality

Zhengping Li, Dong Ding, Sheng Ma, Xunming Deng, and Wenzhong Shen

Abstract High-efficiency and low-cost photovoltaic (PV) technology is considered a top choice toward achieving net-zero carbon dioxide emissions - carbon neutrality. In this Chapter, latest technologies in crystalline silicon (c-Si) PV and the underlined physics and device principles are reviewed. A critical step to achieve high efficiency in c-Si PV is the effective passivation of carrier recombination centres (e.g., dangling bonds) at the surfaces and interfaces, often using silicon-based thin film layers. Based on different approaches to accomplish the passivation, various device structures, such as silicon heterojunction (SHJ) and tunnel oxide passivated contact (TOPCon), are developed and optimized. Other devices structures, including passivated emitter and rear contact (PERC), interdigitated back contact (IBC), combinations of these structures such as TBC, HBC, THBC, and tandem device using perovskite top cell on top of a c-Si bottom cell, are also reviewed and discussed.

1 Introduction

Carbon neutrality is a state of net-zero carbon dioxide emissions. The application of renewable energies can make an important contribution to carbon neutrality. Among renewable energies, photovoltaic (PV) solar energy is a significant answer to the challenges. PV refers to the direct energy conversion of solar radiation into electricity. Solar cells are the key devices for realizing energy conversion. At present, crystalline silicon (c-Si) solar cells are the leading products with a market share of more than 95%. Among c-Si solar cells, tunnel oxide passivated contact (TOPCon) solar cells

Z. Li · D. Ding · S. Ma · W. Shen (✉)
Institute of Solar Energy, and Key Laboratory of Artificial Structures and Quantum Control (Ministry of Education), School of Physics and Astronomy, Shanghai Jiao Tong University, Shanghai, China
e-mail: wzshen@sjtu.edu.cn
URL: https://www.physics.sjtu.edu.cn/jsml/shenwenzhong.html

X. Deng
Department of Physics and Astronomy, The University of Toledo, Toledo, OH 43606, USA

1America Solar, LLC, Toledo, OH 43606, USA

D. Shi (ed.), *Energy Materials Science and Engineering: From New Devices to AI Power Systems*, Green Energy and Technology, https://doi.org/10.1007/978-3-031-88550-1_3

and silicon heterojunction (SHJ, also known as HJT or HIT) solar cells currently have the greatest market shares, and both employ silicon-based thin films as their critical passivation layers to achieve high efficiency.

In this chapter, carbon neutrality and PV are introduced firstly. Then an outline of basic knowledge of semiconductors, p–n junction, solar cells is given. Afterwards, the concept of passivating contact cells is provided. Subsequently, the intrinsic hydrogenated amorphous silicon (i-a-Si:H) thin films and doped silicon films, which constitute the passivated contact stack (i-a-Si:H/doped Si) in SHJ solar cells, are introduced in detail. The stack of silicon suboxide (SiO_x) film and doped polycrystalline silicon (poly-Si) film (SiO_x/poly-Si) forming another passivated contact in TOPCon c-Si cell, is also discussed. At the end, the latest developments in some of the advanced c-Si solar cells—TOPCon/heterojunction hybrid back-contact cell and perovskite/c-Si tandem cell—are briefly introduced. It is anticipated that the readers can learn about the passivated contact c-Si solar cells and the related Si-based thin films in this chapter.

2 Photovoltaic Playing a Dominant Role Towards Achieving Carbon Neutrality

2.1 Current Situation and Trend of Photovoltaic Power Generation

Carbon neutrality refers to a state in which the greenhouse gases emitted into the atmosphere are equivalent to those absorbed from it. In the field of carbon management, carbon emissions generally encompass all greenhouse gas emissions; consequently, carbon neutrality typically refers to the neutralization of all greenhouse gases. To achieve carbon neutrality, two primary approaches exist: reducing carbon emissions and increasing carbon absorption. Reducing carbon emissions necessitates the phasing out of coal-fired, oil-fired, and gas-fired power plants. Currently, 30% of the world's fossil energy is utilized for electricity generation, and eliminating this usage would reduce global carbon emissions by 30%. The phase-out of fossil-fueled power plants must be accompanied by a significant effort to replace them with PV, wind, hydroelectric, and nuclear power, which produce negligible carbon emissions. This transition will subsequently be followed by the gradual conversion of equipment currently utilizing fossil fuels to generate electricity, such as replacing fuel-powered vehicles with electric ones and coal-fired boilers with electric alternatives. Increased carbon absorption is predominantly achieved through carbon capture and storage facilities or via afforestation to augment forest carbon sinks. Forest carbon sinks currently represent the more economically viable method of carbon sequestration and fulfill the dual function of climate change mitigation and adaptation.

Achieving the goal of global carbon neutrality requires vigorous promotion of transition to clean energy. When clean energy consumption accounts for more than

80% of total future energy consumption, solar, wind, hydro, nuclear, hydrogen, and biomass will play significant roles. However, the question arises as to which energy source will play the biggest role in this transition?

The answer is, unequivocally, solar energy.

Solar energy is ubiquitous, and its total available quantity is substantial. It is a sustainable, clean energy source with zero emissions and zero pollution that can be accessed at a relatively low cost. Fundamentally, both traditional fossil energy and newer energy forms such as wind, hydropower, and biomass are derivatives of solar energy, albeit in different forms. Solar energy refers to the direct conversion of solar radiation through photoelectric, photothermal, and photochemical processes. Notably, photoelectric conversion, specifically solar PV power generation, is considered the most promising energy technology.

The PV power generation offers the following advantages:

(1) The most advanced technical principle. Fossil energy requires combustion to convert to heat energy, which is then transformed into electricity; wind and hydropower convert the kinetic energy of wind and water into mechanical energy of the turbines, which is subsequently converted to electricity. In contrast, solar PV power generation directly converts photon energy into electric energy.
(2) Abundant total quantity. The Earth's surface receives daily solar energy equivalent to the energy produced by 100 million barrels of oil. Moreover, the solar energy received by the Earth in a single hour is sufficient to meet human energy consumption for an entire year.
(3) Wide distribution. All regions of the world receive varying degrees of solar irradiation, with certain areas such as North Africa, the Middle East, and the southwestern United States receiving particularly high levels of annual solar irradiation, reaching 10,080, 9720, and 10,512 MJ/m^2, respectively.
(4) Abundant raw material. Silicon, the primary raw material, is highly abundant, constituting 26.4% of the Earth's crust, second only to oxygen.
(5) Broad range of applications. Solar PV power generation can be applied in numerous fields, including aerospace, transportation, agriculture, construction, military operations, and urban lighting. Even remote desert and island locations can benefit from illumination provided by PV power generation.

Solar PV power generation plays an increasingly significant role in our effort to achieve a global carbon emission plateau and carbon neutrality. Among all energy generation and consumption methods, using traditional fossil energy sources such as oil and coal emits 778–960 g of carbon dioxide per kWh of electricity generated, while the carbon emissions from clean energy power generation are all below 45 g/kWh, of which the carbon emissions from solar PV power generation are only 30 g/kWh, less than 1/30 of the carbon emissions from coal-fired power generation. From Fig. 1a [1], it can be noted that the global total power generation in 2014 and 2023 is ~25,000 and ~30,000 TWh, respectively, with an average growth rate of only 2.5% during the 10-year period; whereas solar PV power generation has a compound annual growth rate as high as 50–60%, and its share in the structure of the global total power generation has increased from less than 1% a decade ago to 5.5% in 2023. Figure 1b illustrates the

cost trend for solar PV and conventional thermal power generation [2]. In 2023, the global average levelized cost of electricity (LCOE) of solar PV is $0.044/kWh, which is beginning to be lower than the LCOE of conventional thermal power generation, which is $0.05/kWh, and it will demonstrate a very strong competitiveness in the future of the global energy transition. Figure 1c, d are charts from the International Energy Agency's (IEA) "Renewable Energy Report" released in 2024 [3], covering the current status and future trends of PV power generation. As evident from the charts, more than 5,500 GW of renewable energy capacity will be added globally between 2024 and 2030, almost triple the increase between 2017 and 2023, which translates to approximately 800 GW per year, of which solar PV's share of the total renewable energy capacity will also continue to remain at 60–70% and above. In 2023, China, Europe and the US account for approximately 32%, 20% and 10%, respectively, of the world's total installed renewable energy capacity. While China has the largest installed capacity of new renewable energy, India's growth rate is among the fastest among major economies. Notably, solar PV is expected to triple to more than 16% of the total global power generation mix in 2030 from 2023's 5.5% levels and is expected to further increase its share to 30–40% in 2050.

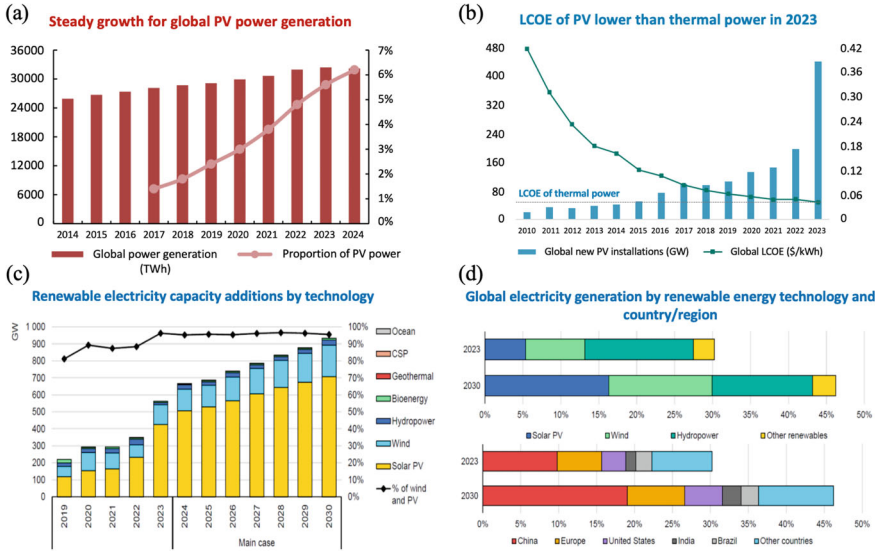

Fig. 1 **a** Global electricity generation and share of PV energy [1]. **b** Trends in global new PV installations and LCOE [2]. **c** Trends in multiple renewable energy generating capacities [3]. **d** Characteristics of the global renewable energy mix and country/region distributions in 2023 (actual) and 2030 (forecast) [3]

2.2 Latest Technologies and Development for c-Si Solar Cells

The primary component of solar PV power generation is the solar cell device. The development of new processes and cell structures aims primarily to enhance cell efficiency by mitigating optical and electrical losses in the PV conversion process. Advanced solar cell technology encompasses numerous aspects, including polycrystalline silicon ingot technology, slicing technology, screen-printed electrode, metal pastes, novel passivation materials, innovative cell structures, and new technologies for modules and power stations, which have significantly reduced the cost of PV power generation. Among the various solar cell products, crystalline silicon (c-Si) solar cells have maintained a market share exceeding 90% for an extended period. The diffusion-doped p–n junction plays a crucial role in the generation and separation of photogenerated carriers in the cell. In the following, the advanced technology and development of solar cells are summarized, focusing on the p–n junction from three perspectives, primarily pertaining to c-Si solar cells.

(1) c-Si solar cells with diffusion-doped p–n junction (homojunction)

In the past few decades, significant progress in c-Si solar cells has come from the technology improving surface passivation. The passivated emitter and rear cell (PERC) structure was developed in 1989 to mitigate the carrier recombination caused by the direct contact between the metal Al and c-Si substrate on the backside of the cell [4]. As illustrated in Fig. 2a, the primary structural features of PERC c-Si solar cells utilize p-type silicon wafers as the substrates, with pyramidal texturing on the front surface and a polished structure on the back surface [5]. High-purity oxygen is passed through methyl chloroform to grow high-quality SiO_2 as the passivation film. The selective emitter structure is prepared using a photolithographic mask method, forming a heavily doped region with a sheet resistance of 20 Ω/sq in the metal–semiconductor contact region, and a lightly doped region with a sheet resistance of 250 Ω/sq. In addition to the localized contact of rear Al and c-Si substrate, the PERC c-Si solar cell employs an $Al/SiN_x/AlO_x$ stack films as the back surface passivation layer and back reflector, which is capable of achieving 97% back reflectance in long wavelengths exceeding 1000 nm. To further enhance the efficiency of PERC cells, researchers proposed passivated emitter and rear locally diffused (PERL) solar cells in 1990 [6], as depicted in Fig. 2b. Its structural improvement primarily involves the preparation of the backside localized contact by diffusing phosphorus sources. The liquid diffusion method has less impact on the lifetime of the c-Si wafer body compared to the solid-state source and spin-coating method for preparing the localized heavy doping. When combined with a front-side Al_2O_3 passivation film, the short-circuit current density (J_{SC}) can be increased by 1.9 mA/cm^2 compared to PERC c-Si solar cells. The tunnel oxide passivated contact (TOPCon) c-Si solar cell in Fig. 2c, completely eliminates direct contact between the back-side metal electrodes and the c-Si wafers [7]. By growing a rear SiO_2 layer with a thickness of only 1–2 nm and subsequently depositing a doped polycrystalline silicon (poly-Si) layer, the two layers together form a passivated contact structure with carrier-selective

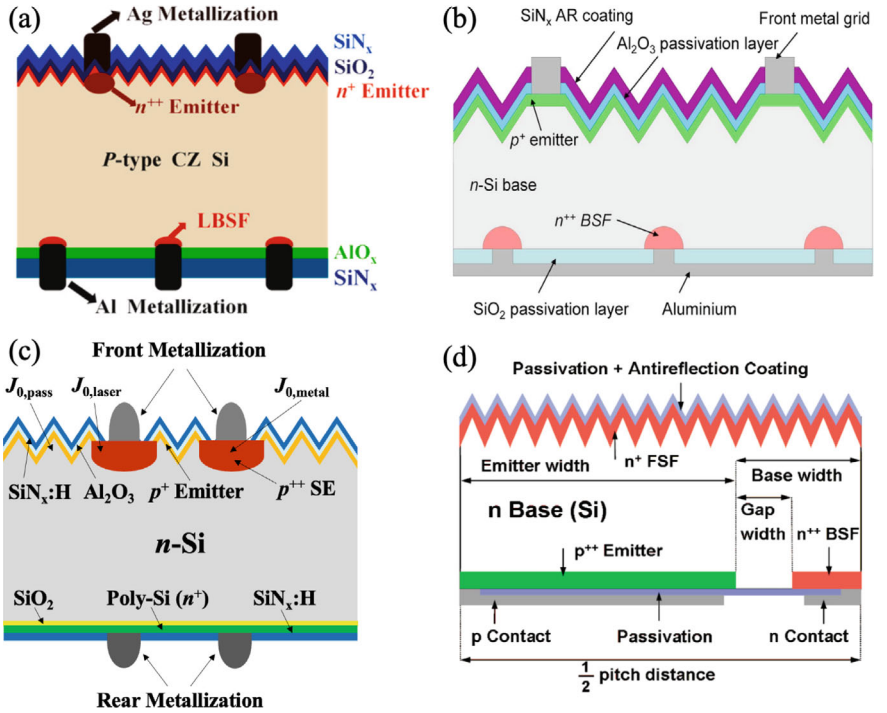

Fig. 2 Schematic diagrams of **a** PERC [5], **b** PERL [6], **c** TOPCon [7], and **d** IBC [8] c-Si solar cell structures

transport capability. The metal grid lines on the front side tend to obstruct part of the incident light. The interdigitated back contact (IBC) c-Si solar cell shown in Fig. 2d relocates all the positive and negative electrodes to the back side [8], allowing the entire frontal area to receive solar irradiation, thereby maximizing the collection of photogenerated carriers.

(2) c-Si solar cells without diffusion-doped p–n junction (heterojunction)

Carrier separation is typically considered to be accomplished by the built-in electric field of the cell device, i.e., diffusion-doped p–n junction. However, it has been demonstrated that carrier separation fundamentally relies on the existence of carrier-selective contacts, and the built-in electric field is merely the result of the formation of a certain type of carrier-selective contacts, which theoretically permits the construction of a cell device without a built-in electric field. Silicon heterojunction (SHJ) solar cells, incorporating phosphorus-doped (P-doped) and boron-doped (B-doped) amorphous silicon (a-Si:H) film, can be approximated as a c-Si solar cell without diffusion-doped p–n junction due to the deposition temperature being less than 250 °C, which impedes the doping element from forming an effective diffusion depth. As illustrated

in Fig. 3a [9], the SHJ c-Si solar cell structure is relatively simple and symmetrically distributed. The front side comprises P-doped amorphous silicon and intrinsic a-Si:H (n-a-Si:H/i-a-Si:H/c-Si) to form a field passivation structure, while the back side consists of B-doped amorphous silicon and intrinsic a-Si:H (p-a-Si:H/i-a-Si:H/c-Si) to form the emitter structure. Owing to the superior passivation performance of a-Si:H, SHJ solar cells can be approximated as a diffusion-free p–n junction with the open-circuit voltage (V_{OC}) of SHJ solar cells frequently exceeding 750 mV. Figure 3b depicts the energy band structure of SHJ solar cells for carrier-selective transport.

In addition to heterojunctions formed by doped silicon thin film materials and c-Si substrates that can be utilized as selective contacts, the implementation of certain heterojunctions composed of materials with lower (<4.0 eV) or higher (>5.2 eV) work functions with c-Si wafer also induces band bending on the silicon surface, which facilitates the function of selective contacts. This type of cell is referred to as a dopant-free solar cell, and its structure is schematically represented in Fig. 3c [10]. Materials with electron selective contact function primarily include metal oxides such as TiO_x, MgO_x and metal halides such as LiF_x, MgF_x, which are generally termed electron transport layer (ETL) materials. Materials with hole selective contact function predominantly include metal oxides such as MoO_x, WO_x, VO_x, as well as organic semiconductors such as PEDOT:PSS, which are typically designated as hole transport layer (HTL) materials. By substituting the c-Si substrate of a dopant-free

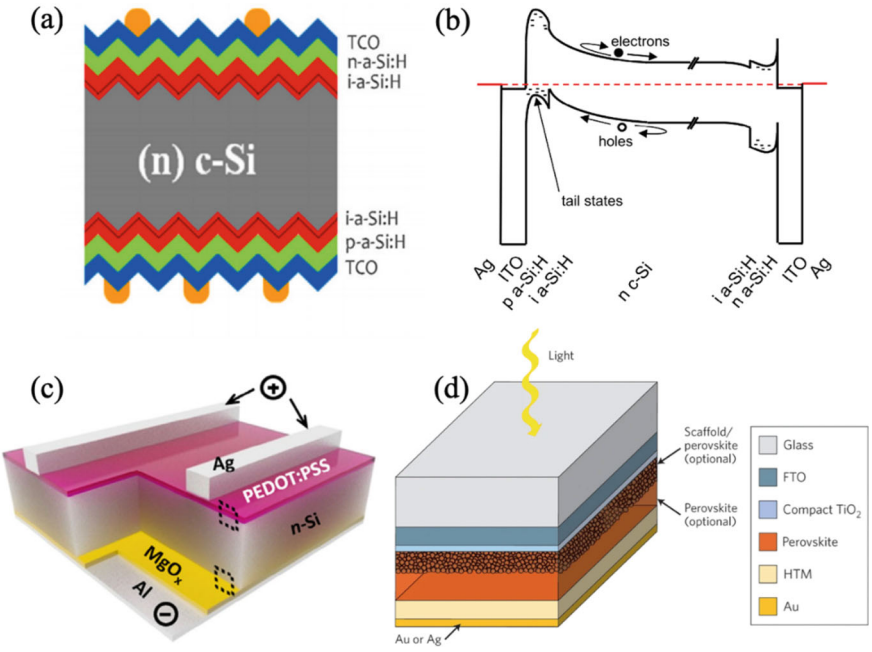

Fig. 3 **a** Schematic structure of SHJ [9] solar cell and **b** energy band structure; **c** Dopant-free [10] and **d** perovskite [11] solar cell structures

solar cell with a perovskite material, a perovskite solar cell is formed, as illustrated in Fig. 3d [11]. Given that the energy bands of perovskite materials are tunable from 1.15 to 3.06 eV, this range allows perovskite materials to exhibit excellent PV conversion performance and broad applicability to sunlight in solar energy. Researches have indicated that the limiting efficiency of single-junction perovskite solar cells is 33%, which significantly surpasses the limiting efficiency of 29.4% for monocrystalline silicon solar cells [12].

(3) Tandem solar cells

To absorb the solar spectrum effectively, semiconductor materials with two different bandgaps are stacked in series on top of each other for effective spectral absorption. Typically, the top wide bandgap material absorbs high-energy photons, while the bottom narrow bandgap c-Si material absorbs low-energy photons. This configuration achieves a broader wavelength absorption region, mitigates carrier heat loss due to energy mismatch, and enables the device to surpass the single junction's Shockley–Queisser limit, thereby realizing high energy conversion efficiency. Compound materials such as GaAs, CdTe, and $CuInSe_2$ can serve as top sub-cells in tandem solar cells. More interestingly, perovskite/c-Si tandem solar cells have been studied since 2015, and their conversion efficiencies have demonstrated remarkable growth from an initial 13.7% [13] to the current 34.6% [14]. Under the irradiation of 1 standard sun, the theoretical conversion efficiencies of the two-junction, three-junction, and infinite junction are 43%, 50%, and 65%, respectively [12, 15–18], assuming 100% radiative compositing and considering solar radiation and electroluminescence. Notably, the theoretically predicted efficiency of the infinite junction cell is 86.8% under a highly concentrated solar spectrum [19, 20].

High efficiency and low cost always are the main subjects of the PV industry. Undoubtedly, higher efficiency solar cells are important for realizing carbon neutrality.

3 Fundamentals of Solar Cells

The photoelectric effect, the conversion of solar radiation to electric energy, is the key point of a solar cell operation. The PV effect of semiconductive materials is the foundation of solar cells. Here, some basic knowledge, including the p–n junction of semiconductors and the working principle of solar cells, is introduced.

3.1 Basis of Semiconductor and p–n Junction

Solid materials can be classified as superconductors, conductors, semiconductors and insulators according to their electrical conductivity. Conductors are materials

with good conductivity, of which the electrical resistivity is below 10^{-5} Ω m. The metals such as the gold, silver, copper, iron, aluminium, are conductors. Insulators are materials with very weak conductivity or even non-conducting, of which the electrical resistivity is higher than 10^{8} Ω m. Such materials like rubber, plastic, wood, and glass are insulators. The electrical conductivity of semiconductors is between those of conductors and insulators, of which the electrical resistivity lies in 10^{-5}–10^{8} Ω m. Elementary substances such as Si (silicon), Ge (germanium), and chemical compounds such as GaAs (gallium arsenide), CdTe (cadmium telluride), are typical semiconductors.

The electroconductibility of solid materials can be interpreted by the band theory. The electrical properties of semiconductors are determined by their electronic band structure. In an insulator, the valence band (the band of electrons that are tightly bound to the atoms) is filled, and the conduction band (the band of electrons that are free to move) is empty. In a conductor, the conduction band is partially filled. In a semiconductor, the conduction band is empty, and the valence band is filled, but there is a small energy gap (E_g) between the two bands.

When a semiconductor is exposed to light or heat, electrons can be excited from the valence band to the conduction band. These electrons are then free to move, and the semiconductor becomes more conductive. This phenomenon is known as intrinsic conduction. Semiconductors can also be doped with impurities to increase their conductivity. Donor impurities add electrons to the semiconductor, while acceptor impurities remove electrons. Doped semiconductors are used to create transistors, diodes, and other electronic devices. Figure 4 is the atomic structure diagram of doping semiconductors.

A p–n junction is a semiconductor interface formed between p-type and n-type materials. This junction is a fundamental building block of many electronic devices, such as diodes, transistors, and integrated circuits. In p-type material, the majority carriers are holes (positive charge carriers), while in n-type material, the majority carriers are electrons (negative charge carriers). At the p–n junction, the differing types of charge carriers combine, resulting in a depletion region where no free carriers exist. This depletion region acts as an insulator, preventing current flow in one direction while allowing it in the other, making the p–n junction diode a critical component for controlling current flow in electronic circuits. The schematic diagram of forming

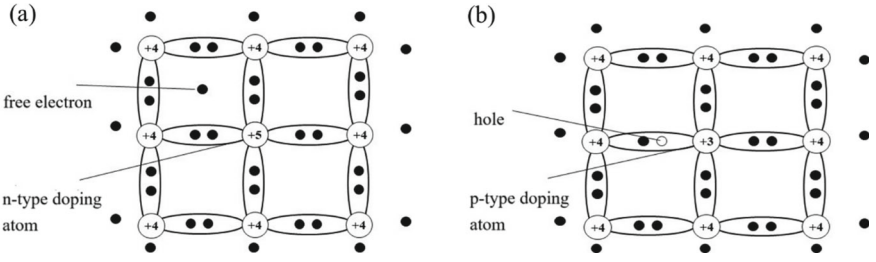

Fig. 4 Atomic structure diagram of doping semiconductors. **a** n-type, **b** p-type

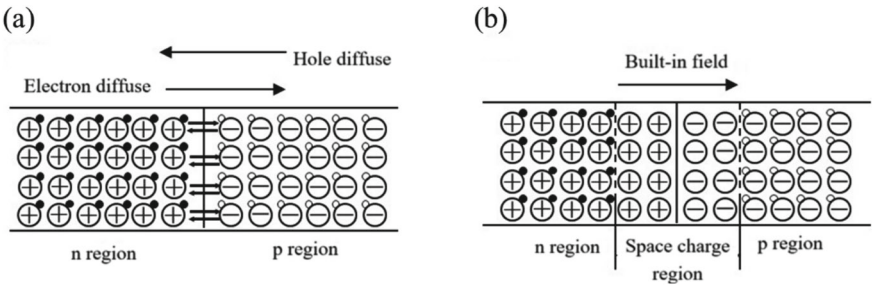

Fig. 5 Schematic diagram of forming a p–n junction. **a** Carriers diffuse before p–n junction formation, **b** space charge region and built-in field after p–n junction formation

a p–n junction can be found in Fig. 5. When a voltage is applied across the junction, the depletion region can either expand or contract, influencing the flow of current. The behavior of the p–n junction can be manipulated to create various electronic components, such as light-emitting diodes (LEDs), solar cells, and bipolar junction transistors (BJTs), making it an essential element in modern electronics. More about semiconductors and p–n junction can be found in book by Sze et al. [21].

3.2 Photovoltaic and Crystalline Silicon Solar Cells

The PV effect, which is the generation of voltage when a device is exposed to light, was discovered by Becquerel [22] in 1839, in a junction formed between an electrode and an electrolyte. Since then, there have been reports of similar effects on different solid-state devices. It was not until 1954 that the solar cell received much-increased interest, initiated by the works of Chapin et al. on single-crystal silicon cells [23]. To date, solar cells have been made with many other semiconductors, using various device configurations, and employing single-crystal, polycrystal, and amorphous thin-film structures.

Solar cells are semiconductor devices that convert light energy into electrical energy. The basic principle behind the operation of a solar cell is the PV effect. When light strikes a semiconductor material, it can excite electrons in the material, causing them to move freely. This movement of electrons creates an electric current, which can be used to power electrical devices. So far, more than 100 kinds of solar cells have been found. The most common type of solar cell is the silicon-based solar cell because silicon is a semiconductor material that is relatively inexpensive and easy to process.

The typical structure of a p-type silicon solar cell is in Fig. 6a. The substrate material is a silicon wafer with a normal thickness of 100–200 μm. The processes for making a crystalline silicon solar cell are shown in Fig. 6b and are described below.

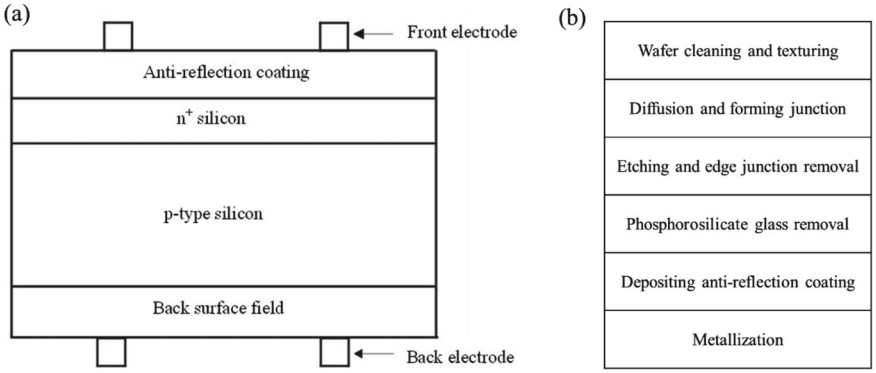

Fig. 6 **a** Schematic structure diagram of a BSF silicon solar cell, **b** processes for a c-Si solar cell fabrication

(1) Wafer cleaning and texturing. The wafer firstly undergoes a wet-chemical etching procedure, e.g. in alkaline potassium hydroxide (KOH) solution, to remove saw damage from the as-cut wafer, and to form light-trapping texture structures (like the pyramids) to enhance anti-reflection properties.
(2) Diffusion and forming junction. The cleaned wafer is put into a diffusion furnace by aerating phosphorus oxychloride ($POCl_3$) to form n^+ silicon layer at a high temperature like 800 °C and above. After that, the p–n junction is formed.
(3) Etching and edge junction removal. The next step is to etch and remove the p–n junction at the edges of the diffused silicon wafer.
(4) PSG removal. A layer of phosphorated silica, called phosphosilicate glass (PSG), has been formed on the surface of diffused silicon wafer. The PSG can be removed by hydrofluoric acid (HF) etching.
(5) Depositing ARC. To enhance the light trapping, a layer of anti-reflection coating (ARC) is deposited by method of plasma-enhanced chemical vapor deposition (PECVD). The ARC is usually hydrogenated silicon nitride (SiN_x:H).
(6) Metallization. Front electrodes are screen printed by using silver (Ag) paste on the front of the silicon wafer. While on the back of the silicon wafer, firstly aluminum (Al) pastes are screen printed to form back surface field (Al-BSF), then back electrodes are screen printed by using Ag paste. After screen printing, the wafers are fired to form an ohmic contact between Ag and Si. Hereto, a silicon solar cell has been prepared. The next is testing and sorting.

3.3 Current–Voltage Characteristics of Solar Cells

A solar cell is assumed to have ideal diode current–voltage (I–V) characteristics. The equivalent circuit is shown in Fig. 7a, where a constant-current source of photocurrent is in parallel with the junction. The source I_{ph} results from the excitation of excess

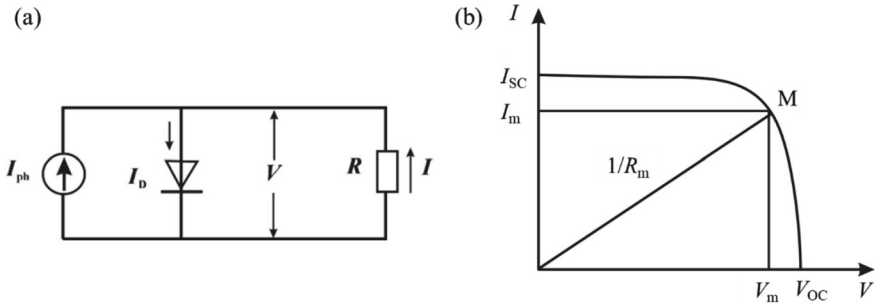

Fig. 7 **a** Ideal equivalent circuit of solar cell under illumination, **b** *I–V* characteristics of a solar cell under illumination

carriers by solar radiation, I_D is dark current which means the current passing through p–n junction with no illumination, and R is the load resistance.

The total *I–V* characteristics of such a device under illumination is simply a summation of the dark current and the photocurrent, given as

$$I = I_D - I_{ph} = I_0\left(\exp\frac{qV}{nkT} - 1\right) - I_{ph} \tag{1}$$

where I_0 is the diode saturation current, q is the electron charge, V is the terminal voltage of the equivalent diode, n is the ideality factor and is generally between 1–2, k is the Boltzmann constant, T is temperature in degree Kelvin.

When the p–n junction is in an open circuit, i.e., the load R is infinity and the current I is zero. From Eq. (1) it can be obtained the open-circuit voltage (V_{OC}) by setting $I = 0$, given as

$$V_{OC} = \frac{nkT}{q}\ln\left(\frac{I_{ph}}{I_0} + 1\right) \tag{2}$$

When the p–n junction is in short-circuit, i.e., the R, V, and I_D are all equal to 0, it can be obtained the short-circuit current (I_{SC}). I_{SC} can be derived from Eq. (1) as.

$$I_{SC} = I = I_{ph} \tag{3}$$

V_{OC} and I_{SC} are the key parameters to characterize a solar cell, which increase with the increase of solar radiation. The V_{OC} and I_{SC} can be obtained by measuring the *I–V* curve of a solar cell under standard test conditions (STC), i.e., solar spectral irradiance distribution of AM1.5G, irradiance level of 1,000 W/m^2, and cell temperature of 25 °C. Like in Fig. 7a, a variable resistance R is connected between positive and negative ends of a cell. Under definite irradiance level and temperature, the currents passing through R and voltages at both ends of R are tested, along with the value of R varying from zero (i.e., short-circuit) to infinity (i.e., open-circuit). Then a plot

of current–voltage can be obtained. Figure 7b is the schematic diagram of the I–V curve. Any point on the curve is a working point. The connecting line between the original point and the working point is called load line, and the reciprocal of the slope of load line is the value of R. The corresponding values of abscissa and ordinate are the working voltage V and working current I, respectively. The output power of the working point is $P = IV$. By properly choosing a load to R_m in which the area of rectangle is largest, a point M called maximum power point (MPP) can be obtained. I_m, V_m, and R_m, are the optimum operating current, optimum operating voltage, optimum load, respectively. P_m ($= I_m V_m$) is also defined as the maximum power output.

Fill factor (FF) is another key parameter for characterizing solar cells. FF measures the sharpness of the I–V curve and is defined as

$$FF = I_m V_m / I_{SC} V_{OC} \tag{4}$$

The most important aspect of a solar cell is the power conversion efficiency (PCE, η) which is the ratio of maximum power output to the incident power. The η can be described as

$$\begin{aligned} \eta &= \frac{P_m}{P_{in} A} \times 100\% = \frac{I_m V_m}{P_{in} A} \times 100\% = \frac{FF \times V_{OC} \times I_{SC}}{P_{in} A} \times 100\% \\ &= \frac{FF \times V_{OC} \times J_{SC}}{P_{in}} \times 100\% \end{aligned} \tag{5}$$

where P_{in} is the incident power per unit area, A is the area of the solar cell, J_{SC} is the short-circuit current density which is the I_{SC} per unit area.

The basic parameters of solar cells, like I_{SC}, V_{OC}, FF, η, and P_m can be obtained from the I–V curve. Optical properties and electrical properties are optimized to improve the efficiency of a solar cell. The steadily increasing bulk carrier lifetimes of c-Si wafers for application to commercial c-Si solar cells make recombination at the cell surfaces and at the contacts the major fundamental limitation in c-Si cells. The surface passivation based on dielectric layers such as silicon oxide, silicon nitride, aluminum oxide and stacks thereof, has led to the development of passivated emitter and rear cells (PERCs) [24–26]. The passivation based on carrier-selective passivation layers which provide an effective passivation of non-contacted as well as contacted areas of a c-Si solar cell, increases the efficiency potential of c-Si solar cells significantly [27]. The so-called "Tunnel Oxide Passivated Contact (TOPCon)" solar cells which are passivated by a stack of silicon oxide and polycrystalline silicon (poly-Si) [28], is a type of carrier-selective passivation solar cells. Other excellent carrier-selective contacts based on hydrogenated amorphous silicon (a-Si:H) layers are well known as HIT (heterojunction with intrinsic thin layer) [29, 30], which have led to the current record efficiency for c-Si solar cells of 27.3% [31]. In the next sections, the silicon thin films in TOPCon and silicon heterojunction (SHJ) solar cells are discussed.

4 Passivating Contact Solar Cell Technology

In conventional c-Si homojunction solar cells, electron and hole-selective contacts are realized by implementing n-type and p-type doping on both sides of the absorber layer of the c-Si substrate. The direct contact between metal and silicon is inevitably utilized in the localization where carriers need to be exported out of the cell device, and the contact exhibits significant carrier recombination current (J_0) in the range of 10^3–10^5 fA/cm^2, which constitutes the primary limitation to cell efficiency improvement [32, 33]. To mitigate the adverse effects of Schottky contact in the metal region, the concept of passivated contact is introduced. Passivated contact structures comprise of thin film materials such as poly-Si, a-Si:H, silicon oxide, and transition metal oxides that are inserted between the metal electrode and the c-Si substrate. A passivation contact is a structure that facilitates the passage of one type of carrier while impeding the transport of another type of carrier, as evidenced by its differential conductivity for different carrier types.

Passivating contact solar cells generally include SHJ and TOPCon c-Si solar cells, as well as other novel cell structures. Figure 8a illustrates the basic principle of passivation contact for the distribution of the density of defect states (D_{it}) and fixed charge density (Q_f) at the interface of thin film materials [34]. It is observed that a-Si:H and SiO_2 exhibit lower D_{it} values, both below 10^{11}/cm^2 eV, which enables superior chemical passivation; while Q_f serves as the source of field passivation, a layer of positively charged fixed charge exists within a 2 nm range on the SiO_2 side of the c-Si/SiO_2 interface, which is insensitive to the position of the Fermi energy level, and the charge density generally falls within the range of 10^{11}–10^{12} cm^{-2}. If Q_f is reduced from 2×10^{12} to 1×10^{12} cm^{-2}, the corresponding effective surface recombination rate increases by a factor of 8. The value of Q_f is dependent on the surface structure and the preparation process: the fixed charge in the SiO_2 film prepared on different c-Si surfaces varies such that $Q_f(100) < Q_f(111)$; the higher the doping concentration in the silicon near the surface of the SiO_2 layer, the larger the value of Q_f. The a-Si:H deposited by PECVD equipment can be employed for SHJ c-Si solar cells. Also, the a-Si:H can be converted to poly-Si using high-temperature annealing, which constitutes the key material for the preparation of TOPCon c-Si solar cells.

Figure 8b illustrates the fundamental principle of passivated contact with recombination current (J_0) and contact resistivity (ρ_c) distributions [35]. Both P-doped amorphous silicon n-a-Si:H/i-a-Si:H and B-doped amorphous silicon p-a-Si:H/i-a-Si:H achieve a remarkably low J_0 of less than 5 fA/cm^2, whereas P-doped poly-Si/SiO_2 stack can attain a notably low ρ_c of only 0.1 mΩ cm^2. The corresponding J_0 and ρ_c distributions for various combinations of hole-selective and electron-selective contact layer materials are depicted in Fig. 8c [35]. As a result of the optimization of surface passivation and metal electrode/c-Si contact, both SHJ and TOPCon solar cells demonstrate substantially increased efficiency limits, to 28.5% for SHJ solar cells and 28.7% for TOPCon solar cells, which are not significantly different from one another.

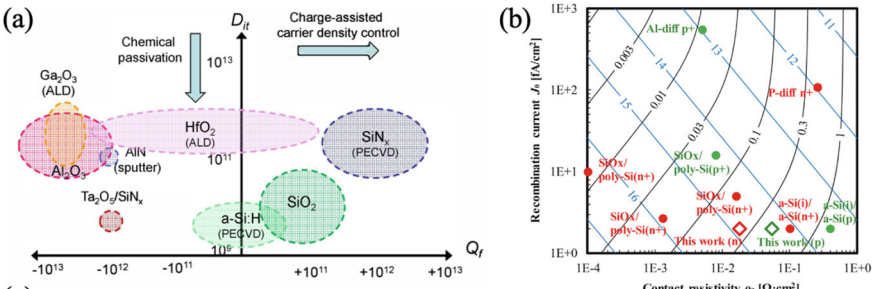

(c)

	Electron selective		P-diffused n+		a-Si:H(i)/a-Si:H(n)		Thermal/PECVD SiO_x/poly-Si(n+)		Thermal/LPCVD SiO_x/poly-Si(n+)		Chemical/LPCVD SiO_x/poly-Si(n+)	
Hole selective			$J_{0,e}$	$\rho_{c,e}$	$J_{0,e}$	$\rho_{c,e}$	$J_{0,e}$	$\rho_{c,e}$	$J_{0,e}$	$\rho_{c,e}$	$J_{0,e}$	$\rho_{c,e}$
			109	0.26	2	0.017	5	0.016	2.7	0.0013	10	0.0001
Al-doped p+	$J_{0,h}$	550	11.7	56.5%	12.9	34.6%	12.8	23.4%	12.9	8.5%	13.0	1.2%
	$\rho_{c,h}$	0.005	3.5%	24.5	1.2%	27.0	1.2%	26.9	1.2%	27.1	1.2%	27.1
a-Si:H(i)/a-Si:H(p)	$J_{0,h}$	2	11.9	45.6%	14.0	24.4%	14.0	14.9%	14.6	5.5%	14.6	0.8%
	$\rho_{c,h}$	0.055	97.9%	24.9	43.9%	28.5	27.6%	28.6	26.2%	28.9	26.0%	28.9
Chemical/PECVD SiO_x/poly-Si(p+)	$J_{0,h}$	16	11.9	46.7%	14.0	23.0%	13.8	15.5%	14.2	5.7%	14.2	0.8%
	$\rho_{c,h}$	0.008	21.4%	24.9	5.9%	28.5	6.1%	28.4	5.8%	28.7	5.7%	28.7

Boxes with blue background: combined selectivity greater than 14
Boxes with pink background: limiting efficiency greater than 28%
Red dotted line: SHJ solar cell
Black dotted line: PERC solar cell
Blue dotted line: p-type TOPCon solar cell
Green dotted line: n-type TOPCon solar cell
Orange dotted line: Bi-facial TOPCon solar cell

Fig. 8 Selective passivation contact fundamentals: **a** interfacial defect states (D_{it}) and fixed charge (Q_f) distribution [34], **b** recombination current (J_0) and contact resistivity (ρ_c) distribution for different tunneling materials [35]; **c** effect of different passivation contact materials on the cell efficiency limit [35]

5 Silicon Thin Films in Silicon Heterojunction Solar Cells

5.1 SHJ Solar Cells

The design of silicon heterojunction solar cell is based on an emitter and BSF that are produced by low-temperature growth of ultra-thin layers of a-Si:H on both sides of a thin c-Si wafer which is less than 200 μm, where electrons and holes are photogenerated. A schematic structure diagram of a silicon heterojunction solar cell is in Fig. 9a. It can be seen that there are three kinds of silicon thin films, i.e., intrinsic amorphous silicon (i-a-Si:H), p-type amorphous silicon (p-a-Si:H), and n-type amorphous silicon (n-a-Si:H). The SHJ solar cells use c-Si wafers for both carrier transport and absorption, and amorphous and/or nanocrystalline thin silicon layers for passivation and junction formation. The top electrode is comprised of a transparent conductive oxide (TCO) layer in combination with a metal grid. The amorphous/crystalline silicon

heterojunction solar cell combines silicon wafer and thin film technologies. Actually, the idea of making solar cells from silicon heterojunction is a rather old one which was published in 1974 by Fuhs et al. [36]. However, it turned out that to realize $V_{OC} > 700$ mV inherent to the heterojunction concept, it is mandatory to include an additional, very thin (of the order of 10 nm) undoped a-Si:H buffer layer between the wafer and doped a-Si:H layers (emitter or BSF). The reason is that the defect density in a-Si:H increases strongly with doping, which leads to high interface defect density at the a-Si:H/c-Si junction, resulting in enhanced recombination and a lower V_{OC}. This finding is the essence of "HIT" concept which is to insert an intrinsic a-Si:H layer between c-Si wafer and doped a-Si:H [29, 30].

In recent years, the structure of SHJ has been developed into a back junction (BJ), i.e., the emitter on the back of the cell. At the same time, the doped layers are nanocrystallized, i.e., n-type hydrogenated nanocrystalline silicon oxide film (n-nc-SiO_x:H) as window layer and p-type hydrogenated nanocrystalline silicon film (p-nc-Si:H) as the emitter. The schematic structure of BJ-SHJ solar cell can be found in Fig. 9b [37]. Figure 9c shows the I–V curve of a BJ-SHJ cell with 26.81% efficiency certificated by the Institute für Solarenergieforschung (ISFH) [37]. There are four major manufacturing processes for SHJ solar cells. The c-Si wafer surface is randomly textured firstly. Secondly, the intrinsic a-Si:H (passivation layers) and doped silicon thin layers (emitter and BSF) are formed by depositing a-Si:H and/or nanocrystalline silicon layers (nc-Si:H) at a temperature below 250 °C in a PECVD

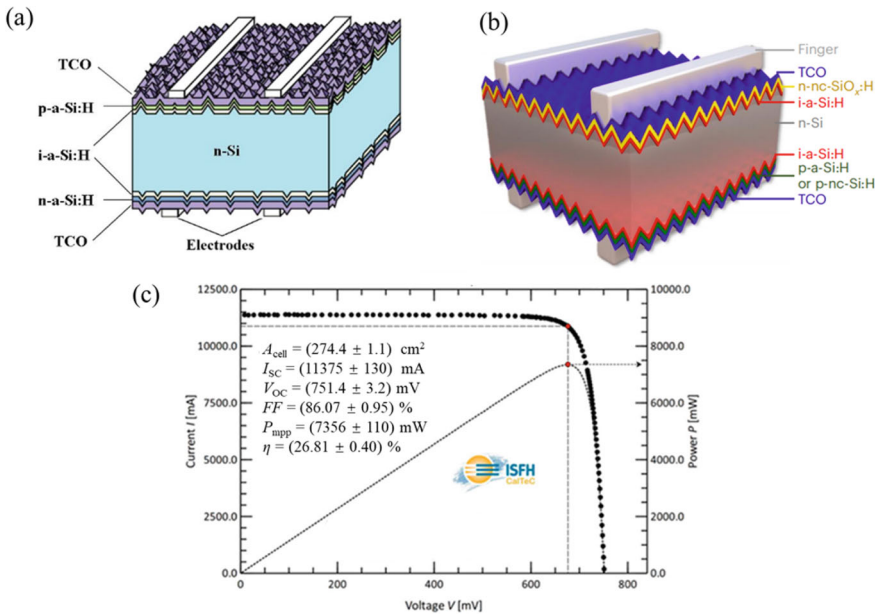

Fig. 9 **a** Schematic structure diagram of SHJ solar cell [30], **b** schematic structure diagram of BJ-SHJ solar cell [37], **c** I–V curve of a BJ-SHJ cell with 26.81% certified efficiency [37]

process. Thirdly, TCO layers are deposited by physical vapor depositing (PVD). Fourthly, silver pastes are screen printed and cured to form grids.

SHJ solar cells have several advantages in comparison to those of homojunction c-Si cells. The structure of SHJ solar cell is symmetric, and the process temperature of SHJ solar cell is typically less than 250 °C, while those of homojunction c-Si solar cells are typically higher than 800 °C. The wafer bowing can be suppressed due to the symmetric structure and low-temperature processes, which enables the use of thinner wafers for cost reduction. The V_{OC} of SHJ solar cell is higher than conventional c-Si cell because of excellent surface passivation. SHJ solar cells also exhibit a smaller drop in performance with increasing temperature in comparison with conventional c-Si cell, which enables SHJ solar cell to generate more power, especially on hot days. The processes of SHJ solar cells include only four major steps, which are simpler and shorter than those of homojunction c-Si cell. However, the processes of SHJ solar cell are totally different from those of homojunction c-Si cells, causing it to require new capital investment for SHJ cell manufacturing.

5.2 Preparation Methods of Silicon Thin Films

Methods of depositing thin films are generally classified as two types, (1) physical deposition, such as evaporation and sputtering, and (2) chemical deposition, like the chemical vapor deposition (CVD). Normally, chemical deposition is applied to obtain the hydrogenated Si thin films. PECVD and hot-wire CVD (HWCVD) are usually used in SHJ processes for depositing Si thin films.

Deposition of Si thin layers, whether they are intended to be used as passivation, emitter or BSF layer, or for material characterization, is usually performed in a parallel plate, mostly capacitively coupled, PECVD system. Figure 10a is the schematic diagram of a PECVD system. It includes a plasma excitation source, matcher, loading system for substrate, heater, vacuum system, gas delivery system and pumping system. In this technique, a plasma occurs during the decomposition of the gaseous precursors, which can be silane (SiH_4), hydrogen (H_2), methane (CH_4), and doping gases such as phosphine (PH_3) and diborane (B_2H_6). During the decomposition, inelastic collision between highly-energetic electrons and the gaseous precursor atoms result in a dissociation into atomic and ionic species [38]. The pathways for the chemical reaction of SiH_4 and its plasma products occurring during the operation of the PECVD system can be found in the literature [39].

The RF (radio frequency) PECVD system operates at a fixed frequency of 13.56 MHz or is driven by a very-high-frequency (VHF) generator, at frequencies ranging up to 110 MHz. Changing the excitation frequency does not necessarily lead to higher deposition rates, but possible changes in the microstructure are likely. The other main factors that affect the deposition rate and structure of resulting Si thin films include plasma excitation power, electrode interspacing, deposition pressure, gas concentration, gas flow, and deposition pressure.

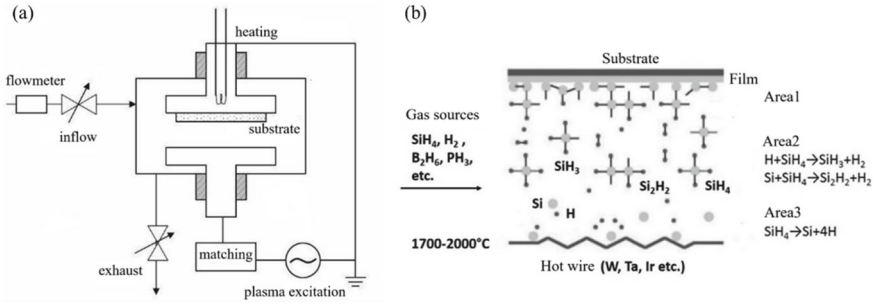

Fig. 10 **a** Schematic diagram of PECVD system, **b** schematic diagram of SiH_4 chemical reactions in HWCVD system [40]

HWCVD is also called catalytic CVD. It is believed that a hot-filament, normally a metal filament (like W, Ta, Ir), acts as a catalytic to decompose the process gas. Figure 10b is the schematics of the SiH_4 chemical reactions in HWCVD for Si thin films [40]. There are three regions in the sketch. The hottest region (Area 3) is near the filament. Typical filament temperatures used in HWCVD roughly vary between 1700 and 2000 °C. Silane decomposes into Si and H when the molecule moves close to the hot wire. In Area 2, the temperature gradient region is between the filament and the substrate. Here, atomic Si and H react with SiH_4 in the gas phase. The majority radials in this region are Si_2H_2 resulting from Si and SiH_4 reaction and some of SiH_3 from H and SiH_4 reaction. The last region (Area 1) is at the substrate surface, where the temperature is constant. Temperature at the surface, to a large degree, determines the structure of the film. Surface reactions and the subsurface release of hydrogen take place at the substrate, after which the silicon matrix relaxes, and the layer is formed. HWCVD is quite different from thermal CVD in that a hot surface absorbs the radicals and deposits the film. There is no film deposition on the hot filament.

HWCVD has several potential advantages compared to PECVD methods. First of all, there are no limitations to the scalability of this technique due to the finite wavelength effect, which is the case in PECVD methods. Secondary, no ions are bombarding the growing film, which could lead to detrimental film properties or damage the film substrates, Thirdly, the substrate holder is not part of the decomposition mechanism, which facilitates the use of moving substrates. Finally, HWCVD has a higher gas utilization compared to PECVD techniques and higher deposition rates can be achieved. Two important drawbacks of the technique are (i) filament ageing and (ii) limited independent control of the substrate temperature due to radiation from the filaments [41].

5.3 Intrinsic Amorphous Silicon Films in SHJ Solar Cells

Figure 11 is the atomic structure sketches of crystalline silicon (c-Si), amorphous (a-Si,) and hydrogenated (a-Si:H) [42]. The well-defined band structure of c-Si principally stems from their lattice periodicity. The diamond like crystal structure results from the formation of strongly directional covalent hybrid bond orbitals. To create a surface, bonds need to be broken, thus the so-called dangling bond (DB) are created. The DBs of c-Si can only exist at the dislocation line (Fig. 11a). For the a-Si, the DBs are formed because of the non-perfect network structure (Fig. 11b), i.e., short-range order while long-range disorder of Si atoms. In Fig. 8c, the DBs are passivated because of the incorporation of H atom in a-Si:H.

On the surface of c-Si, an atom gives rise to a half-saturated DB. The electronic structure of DB gives rise to a surface state within the bandgap [43], which is called recombination center. To resolve surface recombination through DBs, a layer of intrinsic hydrogenated amorphous silicon film is inserted between doped a-Si:H and c-Si to passivate the interface in SHJ solar cell. The physical passivation mechanism of i-a-Si:H stems from chemical surface passivation by hydrogen, similar to defect passivation in the a-Si:H bulk. Intrinsic amorphous silicon films have been known already for some decades to yield good c-Si surface passivation [44].

The DB density changes from 10^{15} to 10^{8} cm^{-2} after i-a-Si:H passivation, thus the silicon wafer gets a longer effective carrier lifetime (τ_{eff}) [45], which may result in a large V_{OC} of SHJ solar cell. This is the reason that the structure of i-a-Si:H film is vital to the V_{OC} and efficiency of SHJ solar cell. Fourier transform infrared absorption (FTIR) spectrum can be used to analyze the structure of a-Si:H film. In the past, the i-a-Si:H was one layer, resulting in the highest efficiency of 25.1% SHJ solar cells [45]. Nowadays, the i-a-Si:H is bilayers or multilayers. Figure 12a, b are the FTIR spectra of i-a-Si:H bilayers, i.e., the buffer layer and normal i-a-Si:H layer [9]. The FTIR spectra are fitted with two Gaussian-distributed absorption peaks centered at wavenumbers of 2000 cm^{-1} and 2100 cm^{-1}, representing monohydride (Si–H) bond and dihydride ($Si–H_2$) bond stretching modes, respectively [46]. The relative intensities of Si–H and $Si–H_2$ absorption for buffer (Fig. 12a) and normal

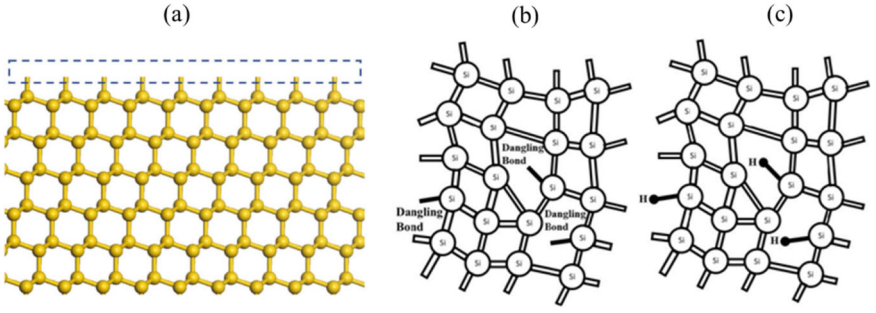

Fig. 11 Structure sketches [42] of **a** c-Si, **b** a-Si, and **c** a-Si:H

i-a-Si:H (Fig. 12b) layers are significantly different. It is observed that there is a greater contribution of Si–H_2 mode in the overall absorption for the buffer layer, implying a higher void density and more disordered hydrogen incorporation within the film [47]. The microstructure factor R^*, is defined as

$$R^* = \frac{I_{2100}}{I_{2000} + I_{2100}} \tag{6}$$

where I_{2100} and I_{2100} are the integral intensity of peak 2000 and 2100 cm^{-1}. The hydrogen in a-Si:H exists mostly in Si–H_2 form if R^* is large, which means that the a-Si:H is porous and has higher void density and richer H content. The a-Si:H film with large R^* is beneficial to passivation of a-Si:H/c-Si interface, while it is not good for the performance of SHJ solar cell. The buffer with high R^* is in a thickness of 0.5–1.0 nm. Then a normal i-a-Si:H with lower R^* which is relatively dense, with lower void density and lower H content, is deposited on the buffer. Furthermore, the normal i-a-Si:H can be divided into two layers, i_1-a-Si:H with moderate R^* and i_2-a-Si:H with lowest R^*. The FTIR spectra and fitness of the triple-layer of i-a-Si:H

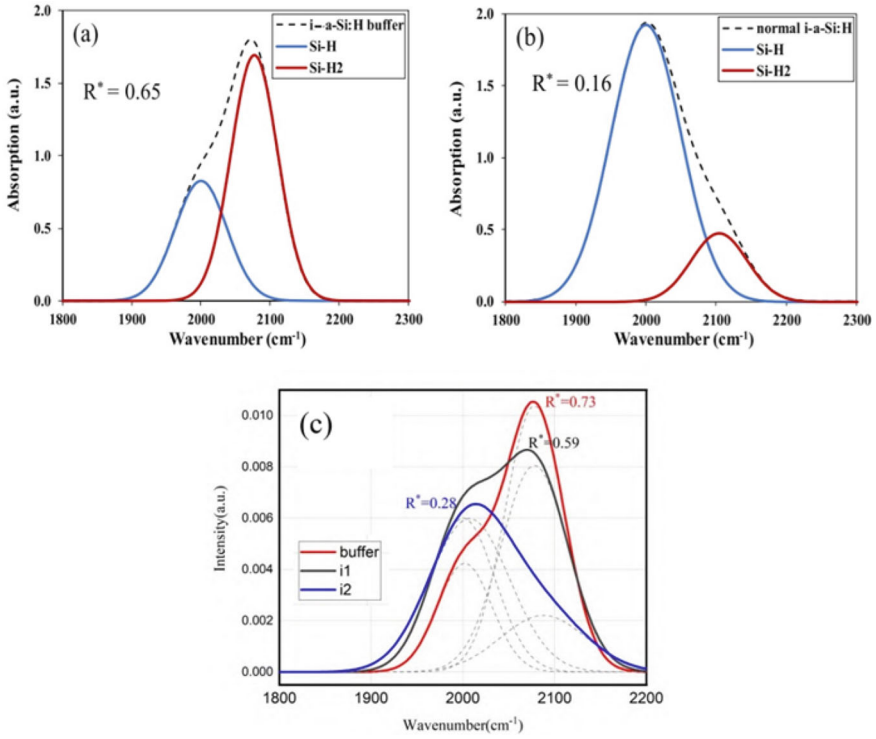

Fig. 12 FTIR spectra fitted by two Gaussian-distributed absorption peaks for **a** buffer, **b** normal i-a-Si:H [9], and **c** triple-layer of i-a-Si:H [48]

[48] is in Fig. 12c. The V_{OC} of around 750 mV for SHJ solar cells can be achieved [37, 48] by using a bilayer or triple-layer structure for i-a-Si:H at the a-Si:H/c-Si interface, which demonstrates the excellent passivation using i-a-Si:H.

A necessary condition for the improvement of i-a-Si:H/c-Si interface passivation is that the interface is atomically sharp, i.e., abrupt, which means that no epitaxial film should be present at the interface [43]. Controlling the thickness of the buffer layer in a range of 0.5–1.0 nm can lead to an abrupt interface. An i-SiO_x:H buffer layer instead of i-a-Si:H buffer can suppress epitaxy [37, 49]. By using a two-stage composite gradient layer of oxygen-containing amorphous silicon sublayer (a-SiO_x:H) and i-a-Si:H, i.e., i-a-SiO_x:H/i-a-Si:H stack, an extremely high V_{OC} of 761 mV was obtained [49].

In brief, intrinsic hydrogenated amorphous film is a key point for highly efficient SHJ solar cells. The i-a-Si:H near the c-Si interface should be porous and with high H content to ensure excellent passivation. A bilayer or triple-layer of i-a-Si:H is necessary to realize the passivation, and epitaxy growth of i-a-Si:H should be avoided.

5.4 Doped Silicon Films in SHJ Solar Cells

To fabricate heterojunction devices, doped films are required to form the emitter and BSF (or front surface field, FSF). Doped a-Si:H layers are usually deposited in similar plasma systems as the intrinsic layers, where for p-type layers either trimethylboron (TMB) or B_2H_6 is mixed in the SiH_4 gas flow, and for n-type films, PH_3 is used. These dopant gases are generally strongly diluted in H_2.

Doping occurs by the incorporation of substitutional impurities. For any semiconductor, intentional doping turns out to form defects; this is a fundamental nature of a semiconductor. It is generally considered that Si–H bond rupture results in defect formation. The formation of defects can be expressed as [50]

$$\mathrm{Si{-}H} \leftrightarrow \mathrm{Si{-}H{-}Si} + \mathrm{Si_{DB}} \tag{7}$$

where Si_{DB} means dangling bond.

Although doped films principally produce a field effect at the interface with c-Si wafer, their electronic passivation properties are often found to be inferior to those of intrinsic films, because the defects formation can lead to reduced passivation at the a-Si:H/c-Si interface. An example of the difference in passivation quality between intrinsic and doped a-Si:H films can be seen in Fig. 13a [51]. In Fig. 13a, τ_{eff} of samples with layers of device-relevant thicknesses deposited in the processing sequence are shown. The structures of samples are i-a-Si:H/c-Si/i-a-Si:H, n-a-Si:H/i-a-Si:H/c-Si/i-a-Si:H/p-a-Si:H, and n-a-Si:H/c-Si/p-a-Si:H, respectively. All results represent films in their as-deposited state (without any postdeposition annealing), deposited on random-pyramid textured c-Si wafers of 200 μm thickness. Despite higher defect densities in progressively thinner films, minority carrier lifetimes as

high as 7 ms (at an excess carrier density of 10^{15} cm^{-3}) were obtained with intrinsic films as thin as 15 nm. The excess carrier density of the sample under 1-sun illumination at V_{OC} conditions is marked by an open circle in the figure. The implied-V_{OC} (iV_{OC}) is defined as the energetic distance between the electron and hole quasi-Fermi levels. An implied-V_{OC} value of 738 mV is obtained at 1 sun for the intrinsic layers shown. Doped films deposited directly on c-Si wafer surfaces provide much poorer passivation. Figure 13a shows a lifetime curve for a sample with 15 nm thin p- and n-type layers deposited on the wafer surfaces. At an excess carrier density of 10^{15} cm^{-3}, a carrier lifetime of less than 0.1 ms is obtained. Under 1-sun illumination, this corresponds to an implied-V_{OC} value of only 613 mV. Similarly, SHJ devices with doped films deposited directly either on n- or p-type c-Si surfaces were limited by their low V_{OC} values. Such drastic passivation loss is almost certainly related to doping-related defect generation in the amorphous host matrix. This effect is most severe for p-type films, but can also play a role in n-type films. Note that this effect is not so much caused by the presence of dopant atoms in the a-Si:H material, but rather due to the shift of the Fermi level away from midgap [52]. Such a shift can significantly lower the formation energy of native defects that counteract intentional doping. Increased doping may thus lead to higher defect densities, which ultimately pin the Fermi level.

Due to such defect formation, it is challenging to simultaneously fulfill both the surface passivation and doping requirements. For this reason, a few-nanometer-thick intrinsic layer is typically inserted between the c-Si surface and the doped a-Si:H films for device fabrication, as was first demonstrated by Sanyo [29]. The benefit of inserting an intrinsic layer underneath the doped layers is clearly demonstrated by the data in Fig. 13a for a-Si:H stacks with total thicknesses of 25 nm. Again, on one wafer side a p-a-Si:H layer was deposited, while the other side received an n-type film, making this asymmetric structure a SHJ solar cell precursor. At an excess

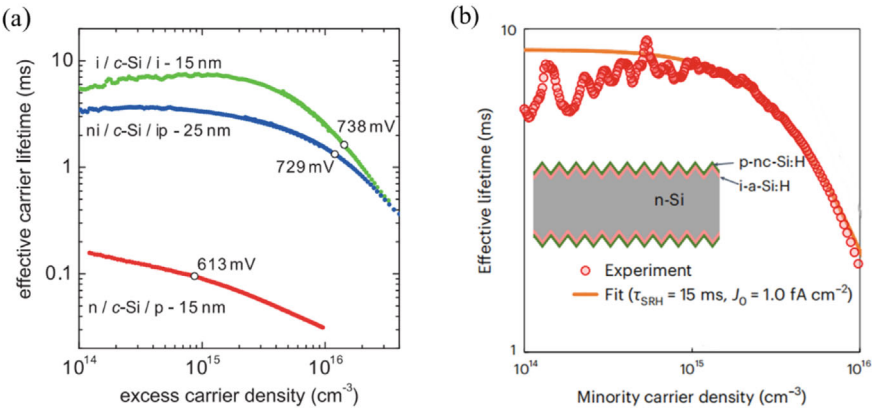

Fig. 13 **a** Effective carrier lifetime and implied-V_{OC} of passivated c-Si wafers consisting of device-relevant a-Si:H stacks [51]. **b** Effective carrier lifetime and structure of p-nc-Si:H/i-a-Si:H/n-Si [37]

carrier density of 10^{15} cm^{-3}, a carrier lifetime higher than 3 ms is obtained. Under 1-sun illumination, this yields an implied-V_{OC} value of 729 mV. The slightly lower passivation quality compared to the case of intrinsic a-Si:H films without doped overlayers may be explained either by defect formation in the intrinsic layer induced by the p-type overlayer, or by probing of the electron wavefunction through the ultra-thin i-layers into the defective doped overlayers.

However, the conductivity of doped a-Si:H is not good enough to transport carriers. The replacement of the p-a-Si:H layer with a p-nc-Si:H layer improves the passivation quality and reduces ρ_c values at both the p layer/i-a-Si:H/n-Si contact and the TCO/p layer interface. The implementation of p-nc-Si:H together with matched TCO leads to a dramatic reduction in the contact resistivity at the rear side, resulting in an efficiency increase in BJ-SHJ cell [37]. Figure 13b is a symmetric structure used to characterize J_0 for the structure based on p-nc-Si:H. The transient mode of a Sinton measurement was used for testing minority carrier lifetime, and the results are indicated by red circles. Tuning the parameters of Shockley–Read–Hall (SRH) recombination (τ_{SRH}, reflecting the quality of silicon wafer) and J_0 (representing the quality of surface passivation), a fitted total J_0 of 1.0 fA/cm^2 is obtained. Considering the symmetry of the structure, it should be 0.5 fA/cm^2 for the J_0 of the p-nc-Si:H/i-a-Si:H/n-Si.

The defect formation because of doping is unavoidable, but its negative impact to the passivation is limited if i-a-Si:H is inserted between c-Si and doped layers. Therefore, the topic for doped a-Si:H is to optimize its optical and electrical properties, not the passivation. However, the lifetime of minority carriers generated in the a-Si:H layers—particularly in the doped layers—is very short so light absorption in these layers is mostly parasitic [51]. This is not a problem at the rear of SHJ cell since the c-Si wafer absorbs all visible light, but light absorbed in the a-Si:H stack at the front of the cell leads to losses of short-circuit current density J_{SC}. The absorption in a-Si:H films in SHJ solar cell is the main factor that results in lower J_{SC} in comparison with TOPCon cell. To minimize the effect of absorption of a-Si:H, the simplest way is to decrease the thickness of a-Si:H layers. However, the a-Si:H layers should be sufficiently thick to achieve passivation and desired field effect.

To improve the J_{SC} of a-Si:H/c-Si heterojunction solar cells further, it is preferable to employ Si-based film as window layer that has larger optical bandgap than a-Si:H to suppress light absorption or to reduce recombination. The doped Si-based films with wide-gap, such as hydrogenated amorphous silicon carbide (a-SiC:H), hydrogenated amorphous silicon-oxygen alloy (a-SiO_x:H), and the nanocryatallized Si-based films like nc-Si:H, nc-SiO_x:H, nc-SiC:H, are all studied.

Investigating the BJ-SHJ structure (see Fig. 9b) which is the mainstream of SHJ nowadays, n-nc-SiO_x:H is employed as a window layer. The external quantum efficiency (EQE) of n-nc-SiO_x:H and n-a-Si:H are shown in Fig. 14a. It can be seen that the parasitic absorption of n-nc-SiO_x:H is less than n-a-Si:H, as illustrated by the improved short-wavelength response. The higher EQE at short-wavelength increases the J_{SC}. Similarly, replacing the p-a-Si:H by p-nc-Si:H, the long-wavelength response is enhanced (Fig. 14b), which is beneficial to J_{SC} improvement. In addition to the improved J_{SC}, the application of doped nc-Si:H or nc-SiO_x:H is also related, to a

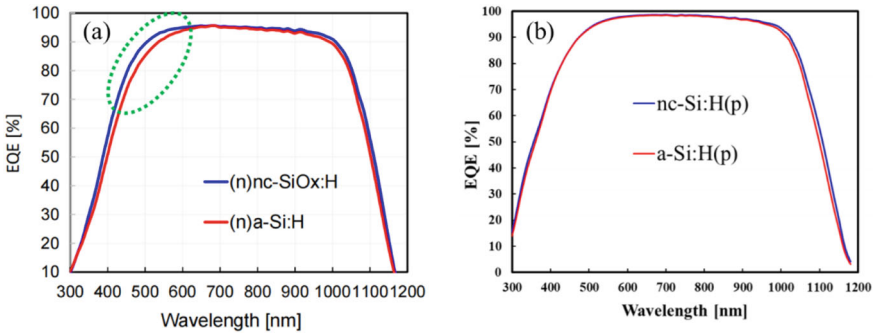

Fig. 14 **a** EQE of n-nc-SiO_x:H versus n-a-Si:H, **b** EQE of p-nc-Si:H versus p-a-Si:H [48]

certain extent, to the achieved high *FF* in SHJ solar cells [53]. The nc-Si:H or nc-SiO_x:H has a higher doping efficiency than a-Si:H, and the dark conductivity can be higher by more than two orders of magnitude than that of doped a-Si:H. The higher doping efficiency also leads to lower series resistances and an adequate nc-Si:H (or nc-SiO_x:H)/TCO electronic contact. The carrier transport properties can be improved because of better conductivity, lower series resistances, and lower contact resistivity with TCO, and hence a higher *FF* of the SHJ devices.

The application of triple-layer i-a-Si:H as passivation layer, n-nc-SiO_x:H as the window layer, p-nc-Si:H as emitter, plus the improved performance of TCO layers and fine screen-printing grids, results in SHJ solar cell with 26.81% efficiency [37]. In 2024, Trina Solar reported an efficiency as high as 27.08% based on n-type SHJ solar cell with fully passivated contact [54]. This is the first time a solar cell efficiency exceeding 27% is achieved using bifacial passivated contact. Besides the excellent passivation of i-a-Si:H films, the key points for improvement of optical and electrical properties of SHJ solar cell include: (1) the optimization of back passivated contact, (2) deposition of doped nanocrystalline silicon by PECVD generated by multi-frequency RF (including VHF) to control the structure and growth rate of doped nc-Si:H, and (3) ultra-fine screen-printed grids.

5.5 Development of HBC Solar Cells

SHJ solar cells have achieved high efficiency due to the application of i-a-Si:H as excellent passivation layers. However, the lower J_{SC} in comparison to TOPCon cell is a drawback for further efficiency improvement. Silicon solar cells usually have grids on both sides so that they are front- and back-contact cells. The grids on the sunny side obstruct light, thus reducing energy input. Placing both terminals on the shaded side creates the so-called back-contact (BC) solar cells that are potentially more efficient. In fact, solar cells with IBC grids, in which the grids are interdigitated on the back side, were introduced in the 1970s [55]. SunPower, established in 1985,

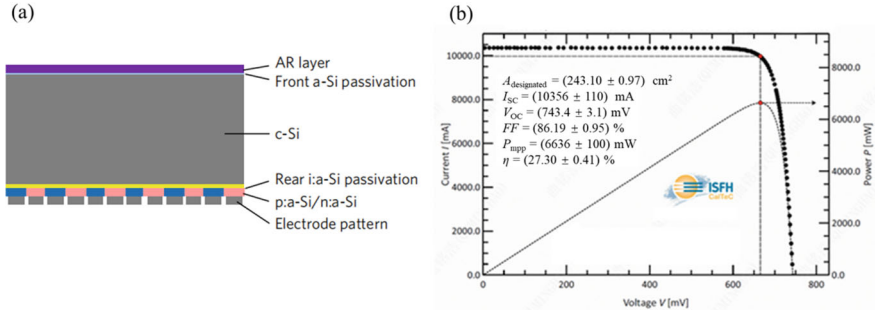

Fig. 15 **a** Schematic structure diagram of HBC solar cell [59], **b** *I*–*V* and power–voltage (*P*–*V*) curves of the 27.3% efficiency HBC cell [31]

became a pioneer in commercializing IBC technology. The IBC structure can also be used together with the SHJ structure to form a heterojunction back-contact (HBC) cell structure which was first developed by Lu et al. in 2007 [56]. Subsequently, companies like Sharp [57], Panasonic [58] and Kaneka [59] have improved HBC technology. In 2017, Kaneka achieved a record 26.7% power conversion efficiency for Si solar cells with the HBC structure [58]. The schematic structure diagram of HBC solar cells can be seen in Fig. 15a [59].

A big challenge in making HBC solar cells is the patterning on the back side, which usually introduces process complexity and power output losses. Although potential solutions have been explored, such as photolithography, inkjet printing, in situ shadow masking and laser patterning, they face technological or cost issues that are still inadequately addressed in mass production. Laser patterning is considered the most economical method for fabricating back-contact solar cells [31]. Pulsed picosecond lasers operating at different wavelengths were used to create the back-contact patterns. Using laser patterning, accompanied with the i-a-Si:H passivation and dense passivating contact technologies, a silicon solar cell with HBC structure has attained an efficiency of 27.3% (V_{OC} = 743.4 mV, J_{SC} = 42.60 mA/cm^2, *FF* = 86.19%) [31]. The *I*–*V* curve of the HBC cell with a 27.3% record efficiency is shown in Fig. 15b.

The low-temperature processes of SHJ and HBC solar cells have a low carbon footprint. Additionally, using laser patterning enhances HBC's performance. The remaining issues are manufacturability and lowering of capital expenditure, to make HBC a prominent terawatt-scale technology for mass production.

6 Silicon Films in TOPCon Solar Cells

The combination of doped poly-Si and tunneling oxide layers has been a focal point of extensive research in both laboratory and industrial settings in recent years. The tunneling oxide plays a crucial role in passivating the c-Si surface, while the doped

poly-Si layer selectively allows the passage of a single type of charge carrier. This concept dates back to the 1980s but gained significant momentum in 2013 when it was incorporated into c-Si solar cells, leading to the development of TOPCon solar cells by Fraunhofer ISE [28]. TOPCon solar cells feature a hybrid architecture on an n-type wafer, incorporating a p^+ emitter and an AlO_x/SiN_x bilayer on the front surface. The rear surface consists of a 1–3 nm thin interfacial SiO_x layer and an n^+ poly-Si layer (Fig. 16a). This design is compatible with the established fabrication processes for PERC solar cells, requiring only additional steps to form the interfacial SiO_x layer, deposit poly-Si, and perform high-temperature annealing and hydrogenation (Fig. 16b). Unlike the PERC architecture with partial-area contacts, the full-area contacts on the rear surface of TOPCon solar cells facilitate one-dimensional vertical transport of charge carriers. The current state-of-the-art stack of SiO_x/n^+ poly-Si contacts is achieved through various deposition and doping techniques, with reported J_0 values below 3 fA/cm^2 and ρ_c below 2 mΩ cm^2 [60]. The excellent passivation contact can primarily be attributed to the synergistic effects of chemical passivation of defects at the c-Si surface and field-effect passivation provided by the doped poly-Si layer. The ultrathin interfacial SiO_x layer plays a key role in saturating dangling bonds on the c-Si surface, thereby reducing the density of interface defects and recombination losses. Simultaneously, field-effect passivation is achieved through high-temperature annealing and crystallization of doped amorphous silicon, which activates the dopant atoms and allows them to diffuse from the poly-Si surface into the c-Si absorber. This results in the formation of a shallow junction at the poly-Si/c-Si interface, creating a strong band bending between the interfaces [61] (Fig. 16c). The SiO_x/n^+ poly-Si stack forms a potential barrier that prevents the migration of minority carriers toward the tunneling oxide, thereby ensuring carrier-selective contact [62]. The superior performance of TOPCon solar cells has driven the exploration of optimal process routes and re-parametrization for the deposition of each functional layer, highlighting the complexity and precision required in fabricating high-efficiency devices [63]. Due to the excellent passivation of SiO_x/n^+ poly-Si stack, combined with the optimization of cell processes, a TOPCon cell with the currently highest efficiency of 26.58% is achieved, and the I–V curve can be found in Fig. 16d.

6.1 Ultrathin Interfacial SiO_x Film

The interfacial SiO_x layer plays a crucial role in TOPCon solar cells, acting as a barrier between the poly-Si layer and the c-Si substrate while also reducing carrier recombination. The quality of interfacial oxides is dependent on the method of preparation. Thermally grown oxides outperform photo-oxidized (UV/O_3) oxides in terms of passivation, even at higher annealing temperatures up to 1000 °C [64]. However, high-temperature thermal oxidation will reduce bulk lifetime, particularly in lower-quality silicon wafers, and the associated high thermal budget may limit its industrial scalability. Wet-chemical oxidation methods, such as nitric acid oxidation (NAOS) and ozone-gas oxidation (wet O_3), present more feasible low-temperature

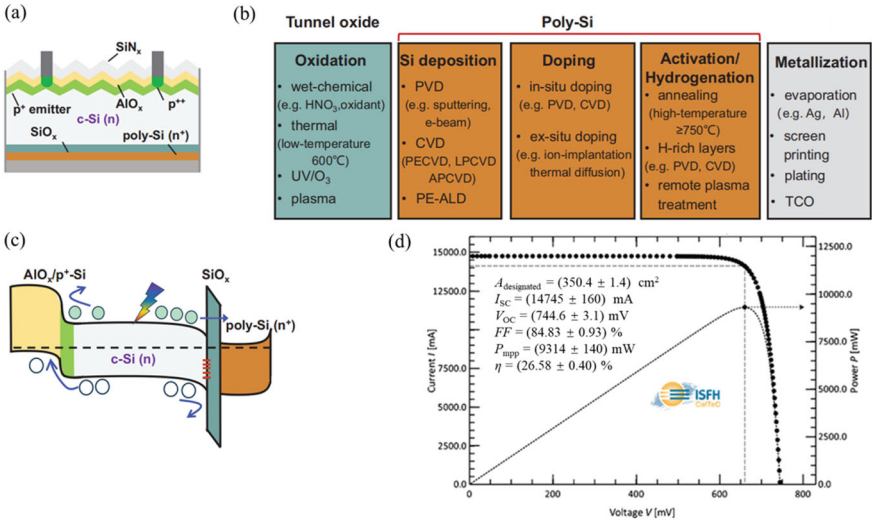

Fig. 16 **a** Structural diagram of a typical n-TOPCon solar cell, showing the layer stack on the front and rear surfaces. **b** Main fabrication steps for TOPCon solar cells, including the deposition of the interfacial SiO_x layer, poly-Si layer, high-temperature annealing, and hydrogenation [63]. **c** Schematic energy band diagram illustrating the band alignment at the poly-Si/c-Si interface and the potential barrier formed by the SiO_x/n^+ poly-Si stack [63]. **d** *I*–*V* curve of a TOPCon cell with 26.58% efficiency

alternatives for growing interfacial oxide layers [65]. These methods have achieved good passivation quality, with iV_{OC} values exceeding 730 mV and J_0 values below 10 fA/cm^2. However, they may face compatibility challenges with in-situ doped thin film silicon growth processes. Plasma-assisted nitrous oxide oxidation (PANO), coupled with PECVD technology, shows promising industrial potential, with iV_{OC} values of 747 mV and 742 mV for n-Si and p-Si, respectively [66, 67]. Additionally, plasma-enhanced atomic layer deposition (PEALD) has been developed for growing interfacial SiO_x, offering precise thickness control down to 2 nm. This method has demonstrated exceptional passivation quality for n-TOPCon cells, with a high iV_{OC} of 759 mV, remarkably low J_0 values of 2.8 fA/cm^2, and a correspondingly low ρ_c value of 0.6 mΩ cm^2 [68].

Several fundamental aspects of the interfacial oxide layer remain the subject of ongoing debate, particularly its thickness, stoichiometry, and charge transport mechanisms. Some researchers have proposed that carrier transport through pinholes might also contribute to the overall transport of the oxide [69]. It is well-established that the thickness of the SiO_x layer plays a crucial role in determining the transport mechanism. For ultra-thin SiO_x layers (<1.7 nm), traditional tunneling models can explain the charge carrier transport [70]. However, tunneling alone cannot account for the low junction resistance observed in thicker SiO_x layers (>2 nm). Interestingly, both tunneling and pinhole-assisted transport mechanisms have been shown to coexist in thin SiO_x layers containing pinholes [71]. While both mechanisms are applicable to some extent, their relative contributions depend on the specific arrangement of

the junctions. Numerical investigations revealed that direct pinhole transport occurs alongside tunneling charge carrier transport at the poly-Si/SiO_x/Si junctions. As shown in Fig. 17 [72], the morphology of the oxide layer is significantly affected by the annealing process. Transmission electron microscopy (TEM) and energy-dispersive x-ray spectroscopy (EDS) were used to assess film quality and detect pinhole formation. Figure 17f illustrates the formation mechanism of pinholes during the annealing step, where the poly-Si and SiO_x films, along with the Si substrate, expand due to the increasing annealing temperature. The poly-Si and Si substrate expand more than the SiO_x film due to their higher thermal expansion coefficients. Tensile stress leads to concave distortion, eventually causing SiO_x fracture. This fracture, which relieves accumulated tension, forms pinholes. This process is reversed during the cooling phase, where the SiO_x layer contracts less than the poly-Si and Si substrate, leading to increased tensile stress in the SiO_x layer and facilitating further crack propagation, thereby increasing pinhole formation [73].

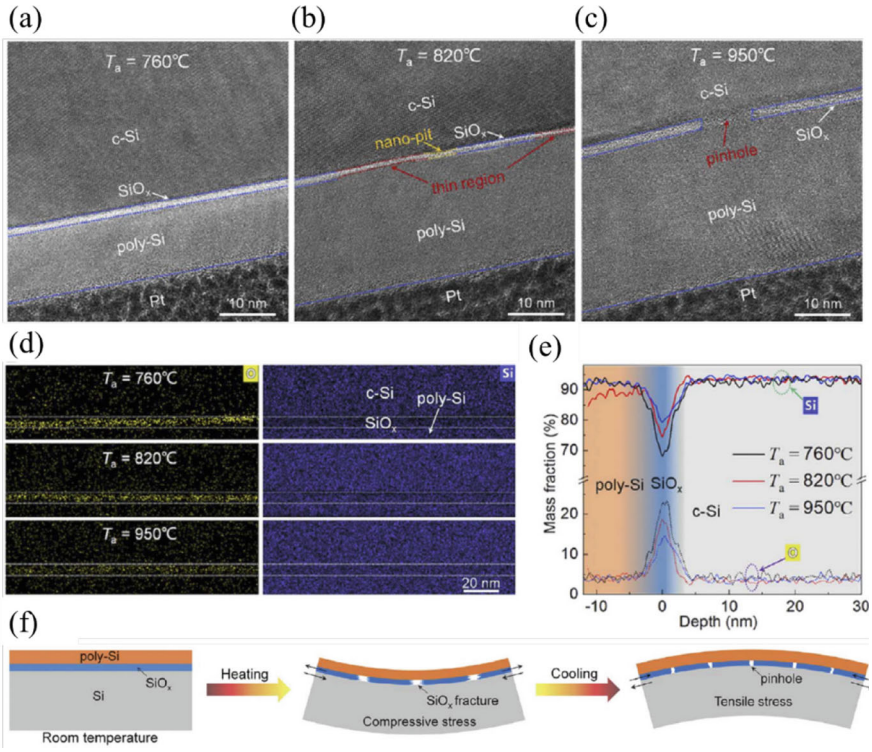

Fig. 17 Appearance of pinholes and their formation mechanism [72]. **a**–**c** Transmission electron microscope (TEM) images of TOPCon structures after high-temperature annealing at T_a = **a** 760 °C, **b** 820 °C, and **c** 950 °C. **d** Local energy dispersive spectroscopy (EDS) profiles. **e** Variation of the mass fractions of Si and O elements with depth. **f** Schematic diagrams illustrating the mechanism of pinhole formation

6.2 Doped Poly-Si Film

The heavily doped poly-Si layer in TOPCon cells serves several crucial functions, including: (1) Contact: the doping concentration of the poly-Si layer plays a significant role in determining the selectivity of the contact. By adjusting the doping levels, the electrical properties of the contact can be optimized, enhancing carrier collection and reducing contact resistance; (2) Barrier against metallization and diffusion: the poly-Si layer acts as a protective barrier, preventing the destruction of the SiO_x passivation layer during metallization and diffusion processes. This helps to preserve the integrity of the passivation, which is essential for reducing recombination losses and maintaining high efficiency; (3) Gettering: the heavily doped poly-Si layer improves the bulk quality of the silicon wafer by acting as a gettering layer. This process helps trap and neutralize harmful impurities, thereby enhancing the overall material quality and reducing the defect density, which can otherwise degrade cell performance; (4) Field effect: the doping in the poly-Si layer induces a field effect that generates a charge-rich region on the silicon surface. This charge-rich layer can repel one type of carrier (either electrons or holes), which contributes to reducing recombination at the surface and improving the overall device efficiency.

In the preparation of the poly-Si layer for the TOPCon solar cells, the dominant approach in industrial applications is low-pressure CVD (LPCVD) of poly-Si, where silane is thermally decomposed in low-pressure quartz tubes. While LPCVD provides high-quality poly-Si films, its non-directional nature necessitates the removal of the poly-Si layer from one side of the wafer, which can detract from the homogeneity and consistency of the process [74]. In contrast, PECVD is a directional deposition method that relies on the plasma-assisted decomposition of precursor gases at low temperatures, which offers several benefits: faster deposition rates, the ability for in situ doping, manageable wrap-around areas that can be easily removed, and the use of graphite boats that can be periodically cleaned without the need for consumables like quartz tubes. Numerous studies have shown that PECVD can achieve comparable performance to LPCVD [75], making PECVD a viable and competitive route for industrial TOPCon cell manufacturing. Dopant incorporation into silicon layers for TOPCon cells can be achieved through various methods. The simplest in situ doping techniques involve introducing controlled rates of dopants, such as PH_3 for n-type or B_2H_6/BCl_3 for p-type, alongside silane during LPCVD or PECVD deposition. However, while this method allows for direct doping during deposition, it is limited by slower deposition rates for doped silicon compared to undoped silicon, and the lateral homogeneity of the doped films is less than ideal. Thermal diffusion, particularly using $POCl_3$ for n-type doping, is the most widely used ex-situ technique in industrial settings. It allows for the simultaneous recrystallization of the silicon layer and activation of the dopants, eliminating the need for a separate high-temperature process. Extensive research has examined how PECVD deposition parameters, such as temperature and deposition power, influence the structural and electrical properties of poly-Si films. For example, higher deposition temperatures reduce Si–H bond concentrations, resulting in denser films that are more conducive to

crystallization during subsequent thermal dopant diffusion processes [76]. However, increasing the thickness of poly-Si films can lead to higher parasitic absorption losses, with a decrease in J_{SC} by approximately 0.15 mA/cm^2 for every 50 nm increase in poly-Si thickness [74].

Doped poly-Si typically exhibits a higher absorption coefficient than c-Si, and its performance is influenced by the doping concentration. Specifically, higher doping levels (above 10^{20} cm^{-3}) can lead to dopant diffusion into the c-Si absorber, which may increase the J_0 and negatively affect the passivation quality [77]. Additionally, high-temperature annealing is often necessary to activate the dopants and promote recrystallization of the poly-Si layer, which is vital for achieving the desired electrical and optical properties. To further improve the optical properties and reduce parasitic absorption, elements like carbon (C), oxygen (O), or nitrogen (N) can be introduced into the poly-Si film. This modification effectively increases the optical band gap of poly-Si, helping to mitigate absorption losses while improving its passivation performance [78]. However, the doping and recrystallization processes generally require specialized, high-cost equipment, and the need for stringent safety protocols due to the involvement of high temperatures and specialty gases. Furthermore, deposition conditions such as gas flow rates, annealing temperatures, and substrate temperatures play a crucial role in determining the quality of the SiO_x/poly-Si junction, doping distribution, and crystallization of the poly-Si layer [79].

6.3 Development of TOPCon Technology

Recent advancements in TOPCon solar cell efficiency have been remarkable, with laboratory-scale efficiencies reaching 25.8% and 26.1% for n-TOPCon and p-TOPCon cells, respectively [80]. Industrial-scale cells have also surpassed 25% efficiency since 2023, with a world record for n-TOPCon cells at 26.58% created by Trina Solar in 2024 [81]. However, efficiency gaps primarily arise from the front surface, particularly the boron-doped p^+ emitter region. Quantitative analysis shows that this area contributes a cumulative loss of 1.19 mW/cm^2, accounting for 63% of the total losses. Optimizing the front surface contact structure is therefore critical for enhancing the performance of TOPCon cells. Figure 18 illustrates the proprietary laser-enhanced contact optimization (LECO) technology, which has been successfully integrated into the pilot production line since 2019 and subsequently scaled up for mass production in 2023. The LECO process, as illustrated in Fig. 18a, involves applying a reverse bias to an already metalized solar cell [82]. A laser scans the cell surface, creating a high density of electron–hole pairs. These pairs are then directed through tiny contact areas between the silicon and the metal surface, resulting in the formation of unique contact structures named current-fired contact (CFC) as shown in Fig. 18b [83]. Fellmeth et al. [84] applied the LECO technology on TOPCon solar cells, and the results reveal that LECO improves the metal–semiconductor contact resistivity ρ_c on the boron emitter and the n-TOPCon side from an underfired state of 2.9 and 14.1 mΩ cm^2 to an enhanced state of 1.8 and 2.9 mΩ cm^2. Ultimately,

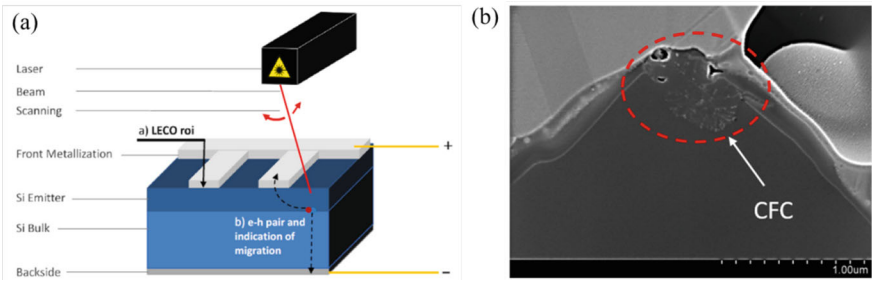

Fig. 18 **a** Schematic diagram of LECO working principle [83]. **b** SEM image of current fired contact (CFC) [84]

LECO improved TOPCon solar cells conversion efficiency by 0.6% compared with the untreated reference.

Other key strategies include adopting a front-surface selective emitter (SE) design, a double-sided TOPCon architecture, and a TOPCon back-contact design (TBC) to minimize efficiency losses [63] (Fig. 19). The contact resistance at the front emitter/metal interface is significant, but it can be substantially reduced using a front-surface SE design. Increasing the doping concentration in the metal contact area helps lower the ρ_c and optimize the J_0 of the front emitter. Another promising option is using a SiO_x/poly-Si passivating contact structure on the front surface, which could push the efficiency to as high as 28.7% [27]. However, careful consideration must be given to the effects of boron doping and the resulting defects. Additionally, the poly-Si layer on the front surface introduces parasitic absorption, requiring limited passivating contact to the front finger area, which increases process complexity. A combined TOPCon and IBC design, the TBC design, is another approach that can further enhance J_{SC} by eliminating the front-contact metal. However, developing metallization techniques compatible with boron-doped poly-Si contacts on the front surface while minimizing costly Ag consumption is a notable challenge. Electroplating technology offers a promising solution by reducing front-surface grid shading, improving cell efficiency, and cutting costs [85]. The choice of metallization scheme is crucial and must align with the doping level and thickness of the poly-Si layer, allowing for adjustments based on the selected metallization techniques and specific requirements.

7 Further Development of Silicon Solar Cells

As the development of TOPCon and SHJ solar cells continues, the highest certified efficiency of single-junction c-Si solar cells has approached their Shockley–Queisser limits of 29.4% [12]. At present, TOPCon is shifted to TBC, while SHJ is shifted to HBC. One trend is that TBC and HBC are merging together as HTBC toward achieving higher efficiency and technological feasibility. On the other hand, to break the efficiency limits of single-junction c-Si solar cells and enrich the application

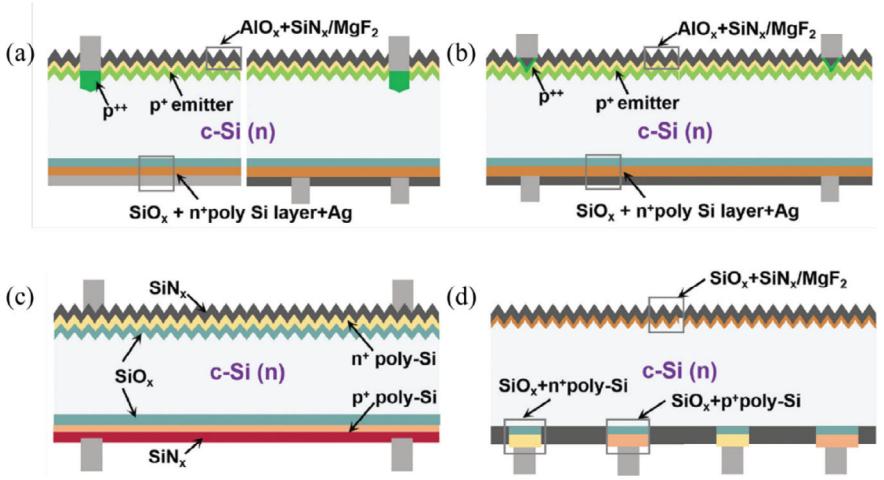

Fig. 19 Development trends of TOPCon solar cells [63], including: **a** optimization of typical n-TOPCon, **b** front-surface SE design, **c** double-sided TOPCon architecture, and **d** TBC design

aspects of PV devices, multi-junction solar cells with a much higher efficiency limit have been intensively studied, of which perovskite/silicon tandem solar cells (TSCs) have attracted special attention because of their potential advantages in efficiency enhancement and cost reduction. In this section, the development trend of silicon solar cells for the above-mentioned two approaches will be discussed.

7.1 TOPCon/Heterojunction Hybrid BC Solar Cells

The i-a-Si:H and doped silicon films in SHJ and HBC solar cells are usually prepared by PECVD. However, the costly use of parallel-plate PECVD limits the spreading and expansion of SHJ and HBC solar cells. Nowadays, TOPCon solar cells with bifacial passivated contact (application of SiO_x/poly-Si on the front side, i.e., poly-finger technology) and with BC electrodes (TBC) are developed. The poly-finger and TBC employ boron-doped polycrystalline silicon (poly-Si(p^+)) as a passivated contacting layer. The preparation of poly-Si(p^+) is not easy, and the passivation of poly-Si(p^+) is not effective. While the i-a-Si:H/p-a-Si:H or i-a-Si:H/p-nc-Si:H in SHJ and HBC solar cells have showed good passivation and technological feasibility, a structure of merging HBC and TBC, which combine p-nc-Si:H or p-a-Si:H with SiO_x/poly-Si(n^+) as p-contact and n-contact, respectively, is developed and called TOPCon/heterojunction hybrid BC (THBC or HTBC) solar cell. A schematic structure diagram of THBC solar cell is shown in Fig. 20a. On the front, the FSF and AlO_x act as passivation layers, while the SiN_x:H is antireflection coating. On the back, c-Si/SiO_x/

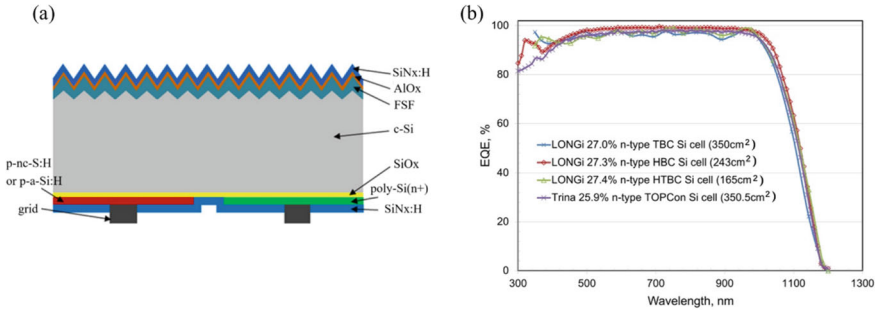

Fig. 20 **a** Schematic structure diagram of THBC solar cell. **b** EQE of THBC cell versus TOPCon, TBC and HBC cells [86]

p-nc-Si:H (or p-a-Si:H) formed the heterojunction and p-type passivating contact, while the SiO_x/poly-Si(n^+) formed the n-type passivating contact.

The THBC solar cell gives a limiting efficiency of 28.9% [35], which shows potential in the future. An efficiency of 27.4% ($V_{OC} = 745.6$ mV, $J_{SC} = 42.35$ mA/cm^2, $FF = 86.7\%$) is reported for a large-area (182 × 91 mm^2) n-type THBC cell, with rear heterojunction p-type contacts and rear TOPCon n-type contacts, fabricated by LONGi Solar and measured by ISFH [86]. The cell, establishing a new record for silicon, has both polarity contacts on the rear surface, restricting loss by the absence of contacts on the front illuminated surface. Figure 20b illustrates the EQE of a THBC cell compared with those of TOPCon, TBC and HBC cells.

7.2 Perovskite/Silicon Tandem Solar Cells

There are many kinds of solar cells. Crystalline silicon solar cells are undoubtedly the dominant ones in the present PV market. Recently, perovskite (PSK) solar cells have attracted much attention, the efficiency of which has been improved from 3.8% [87] to over 26% [88] in the past few years. The combination of perovskite and c-Si, i.e., PSK/c-Si tandem solar cell (TSC) is the most recognized by researchers. The efficiency of PSK/c-Si TSC has soared from 13.7% [13] initially to 33.9% [89] and 34.6% [14] during the past 10 years. According to some studies, the Si bottom-cell with 1.12 eV band-gap stacked with the 1.68 eV PSK top-cell can ensure the optimal absorption of solar spectrum and avoid the thermal relaxation due to the mismatch of band-gap. The theoretical efficiency limit of the full-spectrum matched two-junction PSK/c-Si TSC can exceed 43% [16]. The higher efficiency limit of PSK/c-Si TSC, together with the advantages of the well developed c-Si solar cells technologies, make the TSC widely regarded as one of the most promising future PV technology approaches.

There are currently five options reported in the literature for the preparation of PSK on silicon substrates, including low-cost spin-coating, large-area blade-coating

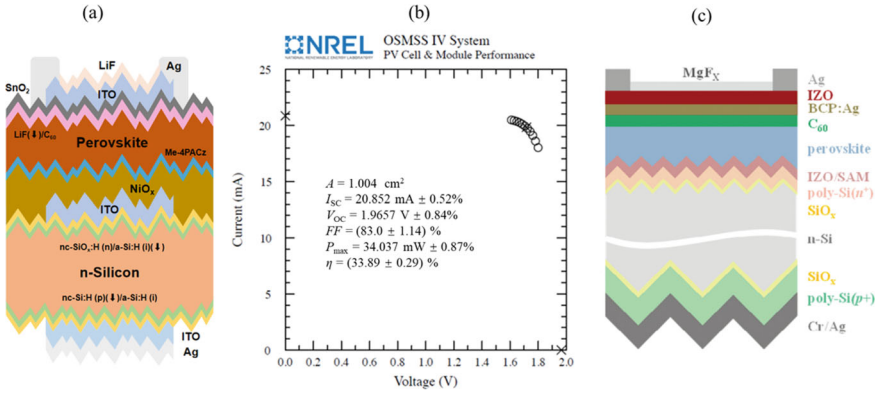

Fig. 21 **a** Schematic structure diagram of PSK/SHJ tandem solar cell, **b** *I–V* curve of a PSK/c-Si TSC with 33.89% efficiency [89], **c** schematic diagram of PSK/TOPCon tandem solar cell [91]

and slot-die coating, facile physical stacking, and excellent conformal co-evaporation + solution. It is worth noting that while co-evaporation + solution is suitable for substrates with various roughness, the complex two-step approach can result in high cost and low performance of PSK/c-Si TSC. In order to obtain PSK films with large area, excellent quality and robust stability, it is essential to explore new simple one-step solution schemes for conformal structures, but this process still requires much further studies [90].

Initially, the PSK/c-Si TSC used an SHJ solar cell as bottom-cell. The schematic structure of PSK/SHJ TSC is shown in Fig. 21a. The *I–V* curve of a PSK/c-Si TSC with 33.89% efficiency certified by the National Renewable Energy Laboratory (NREL) is shown in Fig. 21b. The highest efficiency of PSK/SHJ TSC is 34.6% at present [14]. TOPCon solar cell is also a candidate as bottom-cell for PSK/c-Si TSC. The schematic structure of PSK/TOPCon TSC is shown in Fig. 21c [91]. The highest efficiency of PSK/TOPCon TSC is 33.84% currently [92].

Despite the breakthroughs in cell efficiency, large-scale manufacturing issues, stability issues, and bifacial properties, further research and development is still needed for the adoption of two-terminal (2T) PSK/c-Si TSC in large-scale mass production.

8 Summary

The usage of renewable energies will promote the progress of worldwide carbon neutrality, and PV energy is one of the most important renewable energies. Solar cells are the key devices to realize the conversion of solar energy into electric power. Among the different types of solar cells, c-Si solar cells are dominant, which currently occupy a market share of more than 95%. Surface passivation is the key

point for producing high-efficiency c-Si solar cells. SHJ and TOPCon are the main passivating contact c-Si solar cells.

For SHJ, the key features are that intrinsic hydrogenated amorphous Si films are inserted between c-Si and doped Si layers and the i-a-Si:H/doped Si layers act as passivated contact stack. The i-a-Si:H shows excellent passivation capability. The p-type doped Si layer, either p-a-Si:H or p-nc-Si:H, acts as the emitter. For BJ-SHJ, the n-type doped Si layer, either n-a-Si:H or n-nc-SiO_x:H, acts as the window and front surface field layer. Carefully depositing i-a-Si:H, p-a-Si:H or p-nc-Si:H, n-a-Si:H or n-nc-SiO_x:H are crucial for achieving high-efficiency SHJ cells. In the future, optimal performance of i-a-Si:H and doped Si thin films is beneficial to SHJ and promotes carbon neutrality as the market share of SHJ solar cells increases.

For TOPCon, the stack of interfacial oxide SiO_x and doped polycrystalline films (SiO_x/poly-Si) forms as the passivating contact layers. The excellent passivation contact can primarily be attributed to the synergistic effects of chemical passivation of defects at the c-Si surface and field-effect passivation provided by the doped poly-Si layer. The ultrathin interfacial SiO_x layer plays a key role in saturating dangling bonds at the c-Si surface, thereby reducing the density of interface defects and recombination losses. TOPCon solar cells have been the mainstream device of the present PV industry.

It is clear that Si-based thin films are vital for the high efficiency of c-Si passivating contact solar cells. These high-efficiency solar cells generate more PV power. Widespread use of PV power helps to achieve carbon neutrality in the near future.

Acknowledgements Co-Authors ZL, DD, SM, and WS acknowledge the support of the Major State Basic Research Development Program of China (2022YFB4200101), National Natural Science Foundation of China (11834011 and 11974242), Shanghai New Energy Technology Research and Development Project of 24DZ3000900, and Inner Mongolia Science and Technology Project (Grant No. 2022JBGS0036). Co-Author XD acknowledges support from the University of Toledo and 1America Solar, LLC.

Exercises for this Chapter

1. What proportions of installed photovoltaic and wind power capacity will be in achieving the carbon neutrality, analyzed in terms of electricity generation?

Answer: The average annual growth rate of global electricity generation is 2.5%, while the average annual growth rates of photovoltaic and wind power generation in the past fifteen years are 28% and 14%, respectively. In 2023, the global total electricity generation was about 30 trillion kWh, with photovoltaic and wind power generation contributing 1.6 trillion kWh and 2.3 trillion kWh, respectively. It is anticipated that the annual growth rate of global total electricity generation will remain constant, and global total electricity generation will achieve carbon neutrality by 2060, reaching 74.7 trillion kWh. At fifteen-year intervals, the photovoltaic power generation is projected to reach 11.4, 31.5, and 41.6 trillion kWh in 2038, 2053,

and 2060, respectively. Consequently, the share of photovoltaic power generation in total power generation is estimated to be 56% when global carbon neutrality is achieved. Similarly, the wind power generation is projected to reach 6.3, 11.3, and 13 trillion kWh in 2038, 2053, and 2060, respectively. The share of wind power in total electricity generation is estimated to be 17% when carbon neutrality is achieved.

2. China's annual electricity consumption is currently 10 trillion kWh. Given the present photovoltaic module efficiency of 20%, what area of photovoltaic power plants would need to be installed in the desert regions of western China to meet this demand?

Answer: The standard intensity of solar irradiation on the Earth's surface is 1000 W/m^2. Considering the photovoltaic module's photoelectric conversion efficiency of 20%, the power generated by a 1 m^2 module per hour is 0.2 kWh. Disregarding the effects of nocturnal inactivity and diurnal fluctuations in light intensity, and assuming that solar irradiation in the desert area of western China occurs for 7–8 h per day at standard intensity for 365 days annually, a 1 m^2 module installed in this region would generate ~500 kWh of electricity per year. To meet the 10 trillion kWh electricity demand, the installation of ~20 billion m^2 of modules, or 20,000 km^2 of photovoltaic power plants, would be required in the western desert region.

3. What are the primary factors to be considered in designing a high-performance solar cell?

Answer: The design of a high-performance solar cell necessitates consideration of two principal factors: optical and electrical performance. Optical performance primarily involves the reduction of reflection, transmission, and parasitic absorption losses of incident light, thereby maximizing sunlight absorption by the crystalline silicon substrate. This can be optimized through the pyramid texturing, passivation film material selection, layer quantity, refractive index, and thickness. Electrical properties are predominantly associated with minimizing the recombination loss of photogenerated carriers to enhance carrier collection by the metal electrodes. These properties can be optimized through interface chemical passivation, field effect passivation, and selective contact implementation.

References

1. Fortes P, Simoes SG, Amorim F et al (2022) How sensitive is a carbon-neutral power sector to climate change? The interplay between hydro, solar and wind for Portugal. Energy 239:122106
2. Gorjian S, Sharon H, Ebadi H et al (2021) Recent technical advancements, economics and environmental impacts of floating photovoltaic solar energy conversion systems. J Clean Prod 278:124285
3. International Energy Agency (IEA) Renewables 2024, analysis and forecast to 2030. https://www.iea.org/reports/renewables-2024. Accessed 18 Dec 2024
4. Blakers AW, Wang A, Milne AM et al (1989) 22.8% efficient silicon solar cell. Appl Phys Lett 55:1363–1365

5. Tang HB, Ma S, Lv Y et al (2020) Optimization of rear surface roughness and metal grid design in industrial bifacial PERC solar cells. Sol Energy Mater Sol Cells 216:110712
6. Benick J, Hoex B, van de Sanden MCM et al (2008) High efficiency n-type Si solar cells on Al_2O_3-passivated boron emitters. Appl Phys Lett 92:253504
7. Ding D, Du ZR, Shen WZ et al (2023) Laser doping selective emitter with thin borosilicate glass layer for n-type TOPCon c-Si solar cells. Sol Energy Mater Sol Cells 253:112230
8. Reichel C, Granek F, Hermle M et al (2011) Investigation of electrical shading effects in back-contacted back-junction silicon solar cells using the two-dimensional charge collection probability and the reciprocity theorem. J Appl Phys 109:024507
9. Ru X, Qu M, Wang J et al (2020) 25.11% efficiency silicon heterojunction solar cell with low deposition rate intrinsic amorphous silicon buffer layers. Sol Energy Mater Sol Cells 215:110643
10. Lin H, Ding D, Wang ZL et al (2018) Realization of interdigitated back contact silicon solar cells by using dopant-free heterocontacts for both polarities. Nano Energy 50:777–784
11. Green MA, Ho-Baillie A, Snaith HJ et al (2014) The emergence of perovskite solar cells. Nat Photon 8:506–514
12. Shockley W, Queisser HJ (1961) Detailed balance limit of efficiency of p-n junction solar cells. J Appl Phys 32:510–519
13. Mailoa J, Bailie C, Johlin E et al (2015) A 2-terminal perovskite/silicon multijunction solar cell enabled by a silicon tunnel junction. Appl Phys Lett 106:121105
14. LONGi sets a new efficiency world record of 34.6% for silicon-perovskite tandem solar cells. https://www.longi.com/cn/news/2024-snec-silicon-perovskite-tandem-solar-cells-new-world-efficiency/. Accessed 6 Jan 2025
15. Leijtens T, Bush KA, Prasanna R et al (2018) Opportunities and challenges for tandem solar cells using metal halide perovskite semiconductors. Nat Energy 3:828–838
16. Yu Z, Leilaeioun M, Holman Z (2016) Selecting tandem partners for silicon solar cells. Nat Energy 1:16137
17. Wang J, Li J, Zhou Y et al (2021) Tuning an electrode work function using organometallic complexes in inverted perovskite solar cells. J Am Chem Soc 143:7759–7768
18. Bremner SP, Levy MY, Honsberg CB (2008) Analysis of tandem solar cell efficiencies under AM1.5G spectrum using a rapid flux calculation method. Prog Photovolt Res Appl 16:225–233
19. Araújo GL, Martí A (1994) Absolute limiting efficiencies for photovoltaic energy conversion. Sol Energy Mater Sol Cells 33:213–240
20. Yamaguchi M, Dimroth F, Geisz JF et al (2021) Multi-junction solar cells paving the way for super high-efficiency. J Appl Phys 129:240901
21. Sze SM, Ng KK (2007) Physics of semiconductor devices, 3rd edn. Wiley, New Jersey
22. Becquerel E (1839) On electric effects under the influence of solar radiation. Compt Rend 9:561
23. Chapin DM, Fuller CS, Pearson GL (1954) A new silicon p-n junction photocell for converting solar radiation into electrical power. J Appl Phys 25:676–677
24. Green MA, Blakers AW, Zhao J et al (1990) Characterization of 23-percent efficiency silicon solar cells. IEEE Trans Electron Dev 37:331–336
25. Hoex B, Heil SBS, Langereis E et al (2006) Ultralow surface recombination of c-Si substrates passivated by plasma-assisted atomic layer deposited Al_2O_3. Appl Phys Lett 89:042112
26. Green MA (2015) The passivated emitter and rear cell (PERC): from conception to mass production. Sol Energy Mater Sol Cells 143:190–197
27. Schmidt J, Peibst R, Brendel R (2018) Surface passivation of crystalline silicon solar cells: present and future. Sol Energy Mater Sol Cells 187:39–54
28. Feldmann F, Bivour M, Reichel C et al (2014) Passivated rear contacts for high-efficiency n-type Si solar cells providing high interface passivation quality and excellent transport characteristics. Sol Energy Mater Sol Cells 120:270–274
29. Tanaka M, Taguchi M, Matsuyama T et al (1992) Development of new a-Si/c-Si heterojunction solar cells: ACJ-HIT (artificially constructed junction-heterojunction with intrinsic thin-layer). Jpn J Appl Phys 31:3518–3522

30. Mishima T, Taguchi M, Sakata H et al (2011) Development status of high-efficiency HIT solar cells. Sol Energy Mater Sol Cells 95:18–21
31. Wu H, Ye F, Yang M et al (2024) Silicon heterojunction back contact solar cells by laser patterning. Nature 635:604–609
32. Mader C, Muller J, Eidelloth S (2012) Local rear contacts to silicon solar cells by in-line high-rate evaporation of aluminum. Sol Energy Mater Sol Cells 107:272–282
33. Bullock J, Cuevas A, Samundsett C et al (2015) Simple silicon solar cells featuring an a-Si: H enhanced rear MIS contact. Sol Energy Mater Sol Cells 138:22–25
34. Cuevas A, Allen T, Bullock J et al (2015) Skin care for healthy silicon solar cells. In: IEEE 42nd photovoltaic specialist conference (PVSC), New Orleans, LA, USA
35. Long W, Yin S, Peng FG et al (2021) On the limiting efficiency for silicon heterojunction solar cells. Sol Energy Mater Sol Cells 231:111291
36. Fuhs W, Niemann K, Stuke J (1974) Heterojunctions of amorphous silicon and silicon single crystals. In: Proceedings of the conference on tetrahedrally bound amorphous semiconductors, Yorktown, NY, USA, pp 345–350
37. Lin H, Yang M, Ru X et al (2023) Silicon heterojunction solar cells with up to 26.81% efficiency achieved by electrically optimized nanocrystalline-silicon hole contact layers. Nat Energy 8:789–799
38. Fahrner WR (2013) Amorphous silicon/crystalline silicon heterojunction solar cells. Springer, Berlin Heidelberg, pp 17–19
39. Liebermann MA, Lichtenberg AJ (1994) Principles of plasma and discharges and materials processing. Wiley, New York
40. Wang Q (2009) Hot-wire CVD amorphous Si materials for solar cell application. Thin Solid Films 517:3570–3574
41. Schüttauf JWA (2011) Amorphous and crystalline silicon based heterojunction solar cells. Dissertation, Utrecht University
42. Shen WZ, Gao C, Li ZP (2023) Perovskite/silicon-heterojunction tandem solar cells. Science Press, Beijing (In Chinese)
43. De Wolf S (2012) Intrinsic and doped a-Si:H/c-Si interface passivation. In: van Sark WGJHM, Korte L, Roca F (eds) Physics and technology of amorphous-crystalline heterostructure silicon solar cells. Springer, Berlin Heidelberg
44. Pankove JI, Tarng ML (1979) Amorphous silicon as a passivant for crystalline silicon. Appl Phys Lett 34:156–157
45. Adachi D, Hernández JL, Yamamoto K (2015) Impact of carrier recombination on fill factor for large area heterojunction crystalline silicon solar cell with 25.1% efficiency. Appl Phys Lett 107:233506
46. Tsu DV, Lucovsky G, Davidson BN (1989) Effects of the nearest neighbors and the alloy matrix on SiH stretching vibration in the amorphous SiOr: H ($0 < r < 2$) alloy system. Phys Rev B 40:1795–1805
47. Smets AHM, Kessels WMM, van de Sanden MCM (2003) Vacancies and voids in hydrogenated amorphous silicon. Appl Phys Lett 82:1547–1549
48. Yang M, Ru X, Yin S et al (2022) Progress of high-efficient silicon heterojunction solar cell. In: 18th China solar grade silicon and PV power conference, Taiyuan, China (In Chinese)
49. Li Y, Ru X, Yang M et al (2024) Flexible silicon solar cells with high power-to-weight ratios. Nature 626:105–110
50. van de Walle CG, Street RA (1995) Silicon-hydrogen bonding and hydrogen diffusion in amorphous silicon. Phys Rev B 51:10615–10618
51. De Wolf S, Descoeudres A, Holman ZC et al (2012) High-efficiency silicon heterojunction solar cells: a review. Green 2:7–24
52. De Wolf S, Kondo M (2009) Nature of doped a-Si:H/c-Si interface recombination. J Appl Phys 105:103707
53. Shen WZ, Zhao YX, Liu F (2022) Highlights of mainstream solar cell efficiencies in 2021. Front Energy 16:1–8

54. Trinasolar sets a new efficiency world record of 27.08% for n-type HJT solar cell. http://static.trinasolar.com/cn/resources/newsroom/wed-20241218-2000. Accessed 18 Dec 2024
55. Lammert MD, Schwartz RJ (1977) The interdigitated back contact solar cell: a silicon solar cell for use in concentrated sunlight. IEEE Trans Electron Dev 24(1977):337–342
56. Lu M, Bowden S, Das U et al (2007) Interdigitated back contact silicon heterojunction solar cell and the effect of front surface passivation. Appl Phys Lett 91:063507
57. Nakamura J, Asano N, Hieda T et al (2014) Development of heterojunction back contact Si solar cells. IEEE J Photovolt 4:1491–1495
58. Masuko K, Shigematsu M, Hashiguchi T et al (2014) Achievement of more than 25% conversion efficiency with crystalline silicon heterojunction solar cell. IEEE J Photovolt 4:1433–1435
59. Yoshikawa K, Kawasaki H, Yoshida W et al (2017) Silicon heterojunction solar cell with interdigitated back contacts for a photoconversion efficiency over 26%. Nat Energy 2:17032
60. Nandakumar N, Rodriguez J, Kluge T et al (2019) Approaching 23% with large-area monopoly cells using screen-printed and fired rear passivating contacts fabricated by inline PECVD. Prog Photovolt Res Appl 27:107–112
61. Haug FJ, Ingenito A, Meyer F et al (2019) Contributions to the contact resistivity in fired tunnel-oxide passivating contacts for crystalline silicon solar cells. IEEE J Photovolt 9:1548–1553
62. Richter A, Benick J, Muller R et al (2018) Tunnel oxide passivating electron contacts as full-area rear emitter of high-efficiency p-type silicon solar cells. Prog Photovolt Res Appl 26:579–586
63. Li W, Xu ZY, Yan Y et al (2024) Passivating contacts for crystalline silicon solar cells: an overview of the current advances and future perspectives. Adv Energy Mater 14:2304338
64. Vossen RVD, Feldmann F, Moldovan A et al (2017) Comparative study of differently grown tunnel oxides for p-type passivating contacts. Energy Procedia 124:448–454
65. Moldovan A, Feldmann F, Kaufmann K et al (2015) Tunnel oxide passivated carrier-selective contacts based on ultra-thin SiO_2 layers grown by photo-oxidation or wet-chemical oxidation in ozonized water. In: IEEE 42nd photovoltaic specialist conference (PVSC), New Orleans, LA, USA
66. Huang Y, Liao M, Wang Z et al (2020) Ultrathin silicon oxide prepared by in-line plasma-assisted N_2O oxidation (PANO) and the application for n-type polysilicon passivated contact. Sol Energy Mater Sol Cells 208:110389
67. Rui Z, Zeng YH, Guo XQ et al (2019) On the passivation mechanism of poly-silicon and thin silicon oxide on crystal silicon wafers. Sol Energy 194:18–26
68. Liao B, Wu W, Yeo R et al (2023) Atomic scale controlled tunnel oxide enabled by a novel industrial tube-based PEALD technology with demonstrated commercial TOPCon cell efficiencies> 24%. Prog Photovolt Res Appl 31:220–229
69. Green MA (1978) Effects of pinholes, oxide traps, and surface states on MIS solar cells. Appl Phys Lett 33:178–180
70. Steinkemper H, Feldmann F, Bivour M (2015) Theoretical investigation of carrier-selective contacts featuring tunnel oxides by means of numerical device simulation. Energy Procedia 77:195–201
71. Folchert N, Rienäcker M, Yeo AA et al (2018) Temperature dependent contact resistance of carrier selective Poly-Si on oxide junctions. Sol Energy Mater Sol Cells 185:425–430
72. Zhou J, Su X, Huang Q et al (2022) Recent advancements in poly-Si/SiO_x passivating contacts for high-efficiency silicon solar cells: technology review and perspectives. J Mater Chem A 10:20147
73. Yang Z, Liu Z, Cui M et al (2021) Charge-carrier dynamics for silicon oxide tunneling junctions mediated by local pinholes. Cell Rep Phys Sci 2:100667
74. Fırat M, Radhakrishnan HS, Payo MR et al (2022) Large-area bifacial n-TOPCon solar cells with in situ phosphorus doped LPCVD poly-Si passivating contacts. Sol Energy Mater Sol Cells 236:111544
75. Feldmann F, Steinhauser B, Pernau T et al (2020) Industrial TOPCon solar cells realized by a PECVD tube process. In: 37th European photovoltaic solar energy conference and exhibition, Lisbon, Portugal

76. Chen WH, Truong TN, Nguyen HT et al (2020) Influence of PECVD deposition temperature on phosphorus doped poly-silicon passivating contacts. Sol Energy Mater Sol Cells 206:110348
77. Feldmann F, Muller R, Reichel C et al (2014) Ion implantation into amorphous Si layers to form carrier-selective contacts for Si solar cells. Phys Status Solidi RRL 8:767–770
78. Ingenito A, Nogay G, Stuckelberger J et al (2018) Phosphorous-doped silicon carbide as front-side full-area passivating contact for double-side contacted c-Si solar cells. IEEE J Photovolt 9:346–354
79. Du HJ, Liu ZK, Liu W et al (2023) Concurrently preparing front emitter and rear passivating contact via continuous PECVD deposition plus one-step annealing for high-efficiency tunnel oxide passivating contact solar cells. Sol RRL 7:2201082
80. Zheng PT, Yang J, Wang Z et al (2021) Detailed loss analysis of 24.8% large-area screen-printed n-type solar cell with polysilicon passivating contact. Cell Rep Phys Sci 2:100603
81. Trinasolar unveils i-TOPCon Ultra technology, with cell efficiency of 26.58%. https://www.trinasolar.com/en-mea/resources/newsroom/thu-20241128-2000. Accessed 14 Jan 2025
82. Krassowski E, Jaeckel B, Zeller U et al (2021) Reliability evaluation of PV modules fabricated from treated solar cells by laser enhanced contact optimization (LECO) process. Sol RRL 6:2100537
83. Großer S, Krassowski E, Swatek S et al (2021) Microscale contact formation by laser enhanced contact optimization. IEEE J Photovolt 12:26–30
84. Fellmeth T, Höffler H, Mack S et al (2022) Laser-enhanced contact optimization on iTOPCon solar cells. Prog Photovolt Res Appl 30:1393–1399
85. Grubel B, Cimiotti G, Schmiga C et al (2022) Progress of plated metallization for industrial bifacial TOPCon silicon solar cells. Prog Photovolt Res Appl 30:615–621
86. Green MA, Dunlop ED, Yoshita M et al (2025) Solar cell efficiency tables (Version 65). Prog Photovolt Res Appl 33:3–15
87. Kojima A, Teshima K, Shirai Y et al (2009) Organometal halide perovskites as visible-light sensitizers for photovoltaic cells. J Am Chem Soc 131:6050–6051
88. Yang Y, Chen H, Liu C et al (2024) Amidination of ligands for chemical and field-effect passivation stabilizes perovskite solar cells. Science 386:898–902
89. Liu J, He Y, Ding L et al (2024) Perovskite/silicon tandem solar cells with bilayer interface passivation. Nature 635(2024):596–603
90. Gao C, Du D, Ding D et al (2022) A review on monolithic perovskite/c-Si tandem solar cell: progress, challenges, and opportunities. J Mater Chem A 10:10811–10828
91. Jiang S, Ding Z, Li X et al (2024) Advancing monolithic perovskite/TOPCon tandem solar cells by customizing industrial-level micro-nano structures. Adv Funct Mater 34:2401900
92. Jinkosolar sets a 33.84% efficiency record for perovskite/TOPCon tandem solar cell. https://www.jinkosolar.com/site/newsdetail/2448. Accessed 6 Jan 2025